Supplementary Information for "Roses in the Nonperturbative Current Response of Artificial Crystals"

Christophe De Beule,[1,2] Võ Tiến Phong,[1] and E. J. Mele[1]

[1] *Department of Physics and Astronomy, University of Pennsylvania, Philadelphia PA 19104*
[2] *Department of Physics and Materials Science, University of Luxembourg, L-1511 Luxembourg, Luxembourg*

(Dated: July 28, 2023)

CONTENTS

I. CURRENT RESPONSE TO A UNIFORM ELECTRIC FIELD

We give an overview of the calculation of the steady-state current in a uniform static electric field. We start from the semiclassical equations of motion and the Boltzmann transport equation in the band-projected theory. We then proceed to evaluate this expression by expanding the band dispersion and the Berry curvature in coordination shells.

A. Semiclassical electron dynamics

The semiclassical equations of motion for an electron in a two-dimensional (2D) crystal, occupying an energy band with dispersion $\varepsilon_{n\boldsymbol{k}}$ subjected to a uniform and static electric field $\boldsymbol{E}$ are given by [1, 2]

$$\hbar\dot{\boldsymbol{r}}_{n\boldsymbol{k}} = \nabla_{\boldsymbol{k}}\varepsilon_{n\boldsymbol{k}} - \hbar\dot{\boldsymbol{k}}\times\boldsymbol{\Omega}_{n\boldsymbol{k}}, \tag{1}$$

$$\hbar\dot{\boldsymbol{k}} = -e\boldsymbol{E}, \tag{2}$$

with n the band index and $\boldsymbol{\Omega}_{n\boldsymbol{k}} = \Omega_{n\boldsymbol{k}}\hat{z}$ the Berry curvature, defined as

$$\Omega_{n\boldsymbol{k}} = i\left(\left\langle \frac{\partial u_{n\boldsymbol{k}}}{\partial k_x}\middle|\frac{\partial u_{n\boldsymbol{k}}}{\partial k_y}\right\rangle_{\text{cell}} - \left\langle \frac{\partial u_{n\boldsymbol{k}}}{\partial k_y}\middle|\frac{\partial u_{n\boldsymbol{k}}}{\partial k_x}\right\rangle_{\text{cell}}\right), \tag{3}$$

where $u_{n\boldsymbol{k}}(\boldsymbol{r})$ are cell-periodic Bloch functions in periodic gauge, $u_{n,\boldsymbol{k}+\boldsymbol{G}}(\boldsymbol{r}) = e^{-i\boldsymbol{G}\cdot\boldsymbol{r}}u_{n\boldsymbol{k}}(\boldsymbol{r})$ with $\boldsymbol{G}$ a reciprocal lattice vector, and $\langle u_{n\boldsymbol{k}}|u_{m\boldsymbol{k}}\rangle_{\text{cell}} = \delta_{nm}$. Here we have assumed that terms originating from interband transitions such as the field correction to the Berry curvature [3] can be neglected. In the following, we omit the band index n since we consider a single band.

The current density is given by

$$\boldsymbol{J} = -e\int_{\text{BZ}}\frac{d^2\boldsymbol{k}}{(2\pi)^2}\, f_{\boldsymbol{k}}\dot{\boldsymbol{r}}_{\boldsymbol{k}} \equiv \boldsymbol{J}_{\text{Bloch}} + \boldsymbol{J}_{\text{geom}}, \tag{4}$$

with $e > 0$ the elementary charge and [4]

$$\boldsymbol{J}_{\text{Bloch}} = -\frac{e}{\hbar}\int_{\text{BZ}}\frac{d^2\boldsymbol{k}}{(2\pi)^2}\, f_{\boldsymbol{k}}\nabla_{\boldsymbol{k}}\varepsilon_{\boldsymbol{k}}, \tag{5}$$

$$\boldsymbol{J}_{\text{geom}} = (\hat{z}\times\boldsymbol{E})\,\frac{e^2}{\hbar}\int_{\text{BZ}}\frac{d^2\boldsymbol{k}}{(2\pi)^2}\, f_{\boldsymbol{k}}\Omega_{\boldsymbol{k}}, \tag{6}$$

where $f_{\boldsymbol{k}}$ is the out-of-equilibrium distribution function, obtained from the Boltzmann equation. Note that unlike in the main text, we do *not* add the factor of 2 for spin in the Supplementary Information. In the relaxation-time approximation, the Boltzmann equation is given by

$$\frac{\partial f}{\partial t} + \dot{\boldsymbol{k}}\cdot\frac{\partial f}{\partial \boldsymbol{k}} + \dot{\boldsymbol{r}}\cdot\frac{\partial f}{\partial \boldsymbol{r}} = -\frac{f - f^0}{\tau}, \tag{7}$$

where τ is the momentum-relaxation time and $f^0_{\boldsymbol{k}} = f^0(\varepsilon_{\boldsymbol{k}})$ is the Fermi function,

$$f^0(\varepsilon) = \frac{1}{e^{(\varepsilon-\mu)/k_BT}+1}, \tag{8}$$

with μ the chemical potential and T the temperature. We are interested in the steady-state response of a uniform electric field, such that the first and third term on the left-hand side of Eq. (7) vanish. Hence, we obtain

$$f_{\boldsymbol{k}} - \frac{e\tau}{\hbar}\boldsymbol{E}\cdot\frac{\partial f_{\boldsymbol{k}}}{\partial \boldsymbol{k}} = f^0_{\boldsymbol{k}}, \tag{9}$$

which is formally solved by

$$f_{\boldsymbol{k}} = f^0_{\boldsymbol{k}} + \frac{e\tau}{\hbar}E_i\frac{\partial f^0_{\boldsymbol{k}}}{\partial k_i} + \left(\frac{e\tau}{\hbar}\right)^2 E_iE_j\frac{\partial^2 f^0_{\boldsymbol{k}}}{\partial k_i k_j} + \cdots. \tag{10}$$

For a translational-invariant system, $f^0_{\boldsymbol{k}}$ can be expanded as a Fourier series,

$$f^0_{\boldsymbol{k}} = \sum_{\boldsymbol{R}} f^0_{\boldsymbol{R}}\, e^{i\boldsymbol{k}\cdot\boldsymbol{R}}, \qquad f^0_{\boldsymbol{R}} = \frac{V_c}{(2\pi)^2}\int_{\text{BZ}} d^2\boldsymbol{k}\, f^0_{\boldsymbol{k}}\, e^{-i\boldsymbol{k}\cdot\boldsymbol{R}}, \tag{11}$$

where $\boldsymbol{R}$ are lattice vectors and V_c the area of the unit cell. This yields

$$f_{\boldsymbol{k}} = \sum_{\boldsymbol{R}}\frac{f^0_{\boldsymbol{R}}\, e^{i\boldsymbol{k}\cdot\boldsymbol{R}}}{1 - ie\tau\boldsymbol{E}\cdot\boldsymbol{R}/\hbar}. \tag{12}$$

Plugging this result for the distribution function back into the expression for the currents, we obtain

$$\boldsymbol{J}_{\text{Bloch}}(\boldsymbol{E}) = -\frac{e}{\hbar}\sum_{\boldsymbol{R},\boldsymbol{R}'}\frac{i\boldsymbol{R}' f^0_{\boldsymbol{R}}\varepsilon_{\boldsymbol{R}'}}{1 - ie\tau\boldsymbol{E}\cdot\boldsymbol{R}/\hbar}\int_{\text{BZ}}\frac{d^2\boldsymbol{k}}{(2\pi)^2}\, e^{i\boldsymbol{k}\cdot(\boldsymbol{R}+\boldsymbol{R}')}, \tag{13}$$

$$= \frac{e}{V_c\hbar}\sum_{\boldsymbol{R}}\frac{i\boldsymbol{R} f^0_{\boldsymbol{R}}\varepsilon_{-\boldsymbol{R}}}{1 - ie\tau\boldsymbol{E}\cdot\boldsymbol{R}/\hbar}, \tag{14}$$

$$\boldsymbol{J}_{\text{geom}}(\boldsymbol{E}) = (\hat{z}\times\boldsymbol{E})\,\frac{e^2}{V_c\hbar}\sum_{\boldsymbol{R}}\frac{f^0_{\boldsymbol{R}}\Omega_{-\boldsymbol{R}}}{1 - ie\tau\boldsymbol{E}\cdot\boldsymbol{R}/\hbar}. \tag{15}$$

B. Symmetry properties of the current

We now discuss the constraints put on the currents by symmetry. We start with time-reversal ($\mathcal{T}$) symmetry. In the presence of $\mathcal{T}$, the band dispersion $\varepsilon_{\boldsymbol{k}}$ is an even function of momentum, while the Berry curvature $\Omega_{\boldsymbol{k}}$ is odd. Hence in real space, we have $\varepsilon_{\boldsymbol{R}} = \varepsilon_{-\boldsymbol{R}}$ and $f^0_{\boldsymbol{R}} = f^0_{-\boldsymbol{R}}$, while $\Omega_{\boldsymbol{R}} = -\Omega_{-\boldsymbol{R}}$. We thus see that in a time-reversal-invariant system, $\varepsilon_{\boldsymbol{R}}$ and $f^0_{\boldsymbol{R}}$ are real while $\Omega_{\boldsymbol{R}}$ is imaginary. This then implies

$$\boldsymbol{J}_{\text{Bloch}}(\boldsymbol{E}) \overset{\mathcal{T}}{=} -\boldsymbol{J}_{\text{Bloch}}(-\boldsymbol{E}), \tag{16}$$

$$\boldsymbol{J}_{\text{geom}}(\boldsymbol{E}) \overset{\mathcal{T}}{=} \boldsymbol{J}_{\text{geom}}(-\boldsymbol{E}). \tag{17}$$

Hence, when $\mathcal{T}$ is preserved, the geometric (Bloch) current gives that part of the current that is even (odd) in the electric field.

If the system conserves a crystalline symmetry $\mathcal{S}$, the current obeys

$$\boldsymbol{J}(\mathcal{S}\boldsymbol{E}) \overset{\mathcal{S}}{=} \mathcal{S}\boldsymbol{J}(\boldsymbol{E}). \tag{18}$$

For example, we see that when $\mathcal{C}_{2z}$ $[(x, y) \mapsto (-x, -y)]$ is conserved, the total current is odd in the electric field. In combination with time-reversal symmetry, this implies that the geometric current vanishes, consistent with the fact that the Berry curvature vanishes in that case. Likewise, under a mirror symmetry $\mathcal{M}_x$ ($x \mapsto -x$),

$$J_x(E_x, E_y) = -J_x(-E_x, E_y), \tag{19}$$

$$J_y(E_x, E_y) = +J_y(-E_x, E_y), \tag{20}$$

such that J_x vanishes for $E_x = 0$. Hence a transverse response is forbidden whenever the electric field lies along a mirror axis. In general, the longitudinal and transverse components of the current transform as

$$J_\parallel(\boldsymbol{E}) \equiv \hat{E} \cdot \boldsymbol{J}(\boldsymbol{E}) = \mathcal{S}\hat{E} \cdot \boldsymbol{J}(\mathcal{S}\boldsymbol{E}) = J_\parallel(\mathcal{S}\boldsymbol{E}) \tag{21}$$

$$J_\perp(\boldsymbol{E}) \equiv (\hat{E} \times \hat{z}) \cdot \boldsymbol{J}(\boldsymbol{E}) = \det(\mathcal{S}) J_\perp(\mathcal{S}\boldsymbol{E}), \tag{22}$$

where $\boldsymbol{E} = E\hat{E}$ and $\boldsymbol{J} = J_\parallel \hat{E} + J_\perp \hat{E} \times \hat{z}$. Here we used Eq. (18). Hence, the longitudinal component transforms as a scalar field, while the transverse component transforms as a pseudoscalar field. Note that out-of-plane rotations, such as $\mathcal{C}_{2x}$, act as improper rotations when restricted to the xy plane with $\det \mathcal{S} = -1$.

C. Weak-field expansion

Here we obtain a series expansion in powers of the electric field for the longitudinal and transverse components from symmetry considerations. To this end, we first define the even and odd currents,

$$\boldsymbol{J}^{(\pm)}(\boldsymbol{E}) = \frac{\boldsymbol{J}(\boldsymbol{E}) \pm \boldsymbol{J}(-\boldsymbol{E})}{2}. \tag{23}$$

In the presence of a rotation symmetry about the principal axis $\mathcal{C}_{nz}$ ($n = 2, 3, 4, 6$) of the 2D crystal, we see that the even component is present only for $n = 3$.

In order to implement the symmetry, we need and object that transforms properly under the symmetry. For the rotation symmetry, we consider the object $J_x + iJ_y = Je^{i\theta}$ with $\hat{E} = (\cos\theta, \sin\theta)$. Hence this object transforms as an $L_z = 1$ object under $\mathcal{C}_{nz}$. We first consider the odd component and focus on $\mathcal{C}_{3z}$ symmetry. Up to fifth order in the electric field as, we can write

$$J_x^{(-)} + iJ_y^{(-)} = a(E^2)\,(E_x + iE_y) + b\,(E_x - iE_y)^5 + \mathcal{O}(E^7), \tag{24}$$

where both sides transform as an $L_z = 1$ object. Here we used that L_z is only conserved mod 3 for a system with $\mathcal{C}_{3z}$ symmetry. Incidentally, for a system with $\mathcal{C}_{6z}$, there are no extra terms and we obtain the same expression for the odd current. Here we defined the functions

$$a = a_0 + a_1 E^2 + a_2 E^4, \qquad b = b_0, \tag{25}$$

TABLE S1. Expansions of the currents that are even ($J^{(+)}$) and odd ($J^{(-)}$) in the electric field, up to leading order in the anisotropy, in the presence of $\mathcal{C}_{nz}$ symmetry ($n = 2, 3, 4, 6$). There are additional constraints on the functions $a(E^2)$ and b if $\mathcal{T}$ or other crystalline symmetries are conserved.

	$J_x^{(+)} + iJ_y^{(+)}$	$J_x^{(-)} + iJ_y^{(-)}$
$\mathcal{C}_{2z}$ only	0	$a\,(E_x + iE_y) + b\,(E_x - iE_y)$
$\mathcal{C}_{3z}$	$a(E^2)\,(E_x - iE_y)^2 + b\,(E_x + iE_y)^4$	$a(E^2)\,(E_x + iE_y) + b\,(E_x - iE_y)^5$
$\mathcal{C}_{4z}$	0	$a(E^2)\,(E_x + iE_y) + b\,(E_x - iE_y)^3$
$\mathcal{C}_{6z}$	0	$a(E^2)\,(E_x + iE_y) + b\,(E_x - iE_y)^5$
$\mathcal{M}_x$ or $\mathcal{C}_{2y}$	$ia, ib \in \mathbb{R}$	$a, b \in \mathbb{R}$
$\mathcal{M}_y$ or $\mathcal{C}_{2x}$	$a, b \in \mathbb{R}$	$a, b \in \mathbb{R}$
$\mathcal{T}$	$a = -b^* E^2$	$a \in \mathbb{R}$

with a_0, a_1, a_2, and b_0 c-numbers. We note that $a_0 = \sigma_L + i\sigma_H$ where σ_L (σ_H) is the linear longitudinal (Hall) conductivity. For a system with $\mathcal{T}$ symmetry, a is real because of Onsager reciprocity. Moreover, a mirror or in-plane rotation axis in the y direction, imply that the functions a and b are real. Projecting in the directions parallel $\hat{E} = (\cos\theta, \sin\theta)$ and perpendicular $\hat{z} \times \hat{E} = (-\sin\theta, \cos\theta)$ the electric field, yields

$$J_{\parallel}^{(-)} - iJ_{\perp}^{(-)} \simeq aE + bE^5 e^{-i6\theta}, \tag{26}$$

which, without taking into account any symmetry other than $\mathcal{C}_{3z}$, gives

$$J_{\parallel}^{(-)} \simeq \mathrm{Re}(a_0)E + \mathrm{Re}(a_1)E^3 + [\mathrm{Re}(a_2) + |b_0|\cos(6\theta - \arg b_0)]\,E^5, \tag{27}$$

$$-J_{\perp}^{(-)} \simeq \mathrm{Im}(a_0)E + \mathrm{Im}(a_1)E^3 + [\mathrm{Im}(a_2) - |b_0|\sin(6\theta - \arg b_0)]\,E^5. \tag{28}$$

Note that the *projected* even (odd) current is actually odd (even) in the electric field. We thus find that the anisotropy in the odd current only emerges at fifth order in the electric field. When the system has a mirror axis ($\mathcal{M}_x : x \mapsto -x$) or a rotation symmetry ($\mathcal{C}_{2y}$) about the y axis, this reduces to

$$J_{\parallel}^{(-)} \simeq a_0 E + a_1 E^3 + [a_2 + b_0\cos(6\theta)]\,E^5, \tag{29}$$

$$J_{\perp}^{(-)} \simeq b_0 E^5 \sin(6\theta), \tag{30}$$

where all coefficients are real. One can perform the same analysis for a system with $\mathcal{C}_{2z}$ or $\mathcal{C}_{4z}$ symmetry. For the former, we find

$$J_{\parallel}^{(-)} - iJ_{\perp}^{(-)} = aE + bEe^{-i2\theta} + \mathcal{O}(E^3), \tag{31}$$

and for the latter,

$$J_{\parallel}^{(-)} - iJ_{\perp}^{(-)} = aE + bE^3 e^{-i4\theta} + \mathcal{O}(E^5). \tag{32}$$

Here we expanded up to the lowest order that shows anisotropy.

Similarly, we expand the even part of current up to fourth order in the electric field. Since the even part of the current vanishes in the presence of $\mathcal{C}_{2z}$ symmetry, we only need to consider $\mathcal{C}_{3z}$ symmetry:

$$J_x^{(+)} + iJ_y^{(+)} = a(E^2)\,(E_x - iE_y)^2 + b\,(E_x + iE_y)^4 + \mathcal{O}(E^6), \tag{33}$$

with $a = a_0 + a_1 E^2$ and $b = b_0$. The longitudinal and transverse components become

$$J_{\parallel}^{(+)} - iJ_{\perp}^{(+)} \simeq aE^2 e^{-i3\theta} + b_0 E^4 e^{i3\theta}. \tag{34}$$

In the semiclassical theory, the presence of $\mathcal{T}$ symmetry requires that $J_{\parallel}^{(+)}$ vanishes since the geometric current is purely transversal. This implies that $a_0 = 0$ and $a_1 = -b_0^*$. Moreover, a mirror axis along the y direction further constrains a and b to be purely imaginary. Hence $a_1 = b_0 = -ic$ such that

$$J_{\perp}^{(+)} \simeq 2cE^4 \cos(3\theta). \tag{35}$$

An overview of the weak-field expansions of the even and odd current is given in Table S1.

II. EXPANSION IN COORDINATION SHELLS

In this section, we calculate the current with the semiclassical theory for a single isolated Chern trivial band. This band is part of a larger band manifold but is well-separated from other bands. We further assume that time-reversal ($\mathcal{T}$) symmetry, $\mathcal{C}_{3z}$ rotation symmetry, and $\mathcal{M}_x$ ($x \mapsto -x$) mirror symmetry are preserved, but that $\mathcal{C}_{2z}$ or spatial inversion symmetry is broken. Hence, a finite Berry curvature is allowed even though the Chern number vanishes.

We write the dispersion $\varepsilon_{\boldsymbol{k}}$ and the Berry curvature $\Omega_{\boldsymbol{k}}$ in terms of an expansion in the coordination shells of the triangular lattice:

$$\varepsilon_{\boldsymbol{k}} = \varepsilon_0 + \varepsilon_1 \sum_{n=1}^{3} \cos(\boldsymbol{k}\cdot\boldsymbol{L}_n^{(1)}) + \varepsilon_2 \sum_{n=1}^{3} \cos(\boldsymbol{k}\cdot\boldsymbol{L}_n^{(2)}) + \cdots , \tag{36}$$

$$\Omega_{\boldsymbol{k}} = \Omega_1 \sum_{n=1}^{3} \sin(\boldsymbol{k}\cdot\boldsymbol{L}_n^{(1)}) + \Omega_3 \sum_{n=1}^{3} \sin(\boldsymbol{k}\cdot\boldsymbol{L}_n^{(3)}) + \cdots , \tag{37}$$

where we set $\varepsilon_0 = 0$ from now on. The first coordination shell is given by a regular hexagon whose vertices lie at a distance L from the origin, where L is the lattice constant. Here we choose

$$\boldsymbol{L}_1^{(1)} = \boldsymbol{L}_1, \tag{38}$$

$$\boldsymbol{L}_2^{(1)} = \boldsymbol{L}_2, \tag{39}$$

$$\boldsymbol{L}_3^{(1)} = -\left(\boldsymbol{L}_1 + \boldsymbol{L}_2\right), \tag{40}$$

where $\boldsymbol{L}_1 = L\left(1/2, \sqrt{3}/2\right)$ and $\boldsymbol{L}_2 = L\left(-1, 0\right)$ are primitive lattice vectors. Here we define the lattice vectors such that $\mathcal{C}_{3z}$, i.e., $\boldsymbol{L}_{n+1}^{(j)} = \mathcal{C}_{3z}\boldsymbol{L}_n^{(j)}$ for $j = 1, 2, 3, \ldots$. The second shell is given by a regular hexagon that is rotated by $\pi/6$ with respect to the first shell and scaled by a factor of $\sqrt{3}$, as shown in Fig. 2(a) of the main text. The third shell is given by the first shell scaled by a factor of 2. The corresponding lattice vectors can be chosen as

$$\boldsymbol{L}_1^{(2)} = \boldsymbol{L}_1 - \boldsymbol{L}_2, \tag{41}$$

$$\boldsymbol{L}_2^{(2)} = \boldsymbol{L}_1 + 2\boldsymbol{L}_2, \tag{42}$$

$$\boldsymbol{L}_3^{(2)} = -\left(2\boldsymbol{L}_1 + \boldsymbol{L}_2\right), \tag{43}$$

$$\boldsymbol{L}_1^{(3)} = 2\boldsymbol{L}_1, \tag{44}$$

$$\boldsymbol{L}_2^{(3)} = 2\boldsymbol{L}_2, \tag{45}$$

$$\boldsymbol{L}_3^{(3)} = -2\left(\boldsymbol{L}_1 + \boldsymbol{L}_2\right). \tag{46}$$

The fourth and fifth shells are degenerate, i.e., they both lie at a distance $\sqrt{7}\,L$ from the origin. These shells are given by two regular hexagons that are rotated by an angle $\pi/6 \pm \arctan\left(\sqrt{3}/5\right)$ with respect to the first shell, respectively.

A. Symmetry constraints

Time-reversal symmetry requires an even band dispersion $\varepsilon_{\boldsymbol{k}} = \varepsilon_{-\boldsymbol{k}}$, while the Berry curvature is required to be odd, $\Omega_{\boldsymbol{k}} = -\Omega_{-\boldsymbol{k}}$. Under a crystalline symmetry $\mathcal{S}$, the band dispersion transforms as a scalar, while the Berry curvature transforms as a pseudoscalar:

$$\varepsilon_{\boldsymbol{k}} = \varepsilon_{\mathcal{S}\boldsymbol{k}}, \qquad \Omega_{\boldsymbol{k}} = \det(\mathcal{S})\Omega_{\mathcal{S}\boldsymbol{k}}. \tag{47}$$

Hence, the Berry curvature acquires a sign under $\mathcal{M}_x$ symmetry. This constrains the coefficients ε_j and Ω_j in the expansion in coordination shells, given in Eq. (37). For instance, the second shell in $\Omega_{\boldsymbol{k}}$ does not transform properly under $\mathcal{M}_x$, instead it transforms properly under $\mathcal{M}_y$. Hence we set $\Omega_2 = 0$ in Eq. (37). This can be understood from the shell structure shown in Fig. 2(a) of the main text. For the 2nd shell, there are two lattice vectors that are related by both $\mathcal{C}_{3z}$ and $\mathcal{M}_x$ symmetry, such that the corresponding term of the Berry curvature will be even under $\mathcal{M}_x$. The 3rd shell, however, is merely a rescaled version of the 1st shell and Ω_3 can be therefore be finite. Similarly, only antisymmetric superpositions of the fourth and fifth shells are allowed, i.e., $\Omega_4 = -\Omega_5$. Conversely, the band dispersion requires a symmetric superposition of the 4th and 5th shells to conserve $\mathcal{M}_x$ symmetry, i.e., $\varepsilon_4 = \varepsilon_5$.

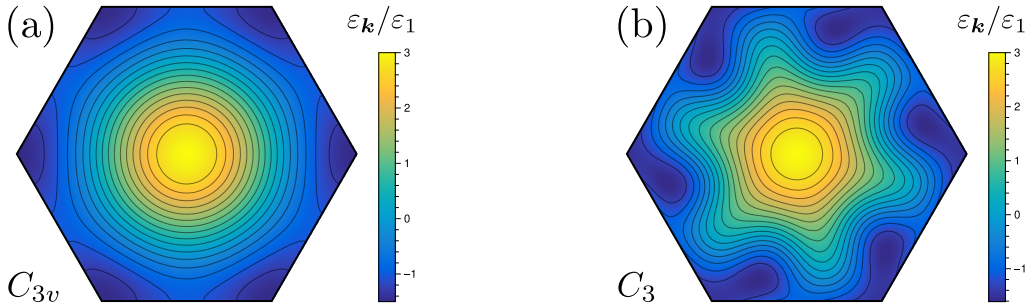

FIG. S1. Energy bands with $\mathcal{C}_{3z}$ and $\mathcal{T}$ symmetry. (a) First-shell approximation, i.e., only ε_1 is finite such that $\mathcal{M}_x$ is conserved. (b) Including higher shells that explicitly break $\mathcal{M}_x$ symmetry, $\varepsilon_4/\varepsilon_1 = -\varepsilon_5/\varepsilon_1 = 0.2$.

Hence, we need to expand up to the 4th and 5th shells to break $\mathcal{M}_x$ in the band dispersion, while we only need to expand up to the 2nd shell to break $\mathcal{M}_x$ in the Berry curvature. Similar relations hold for higher-order shells.

We show the energy band in the first-shell approximation in Fig. S1(a) and including the 4th and 5th shell with opposite coefficients such that $\mathcal{M}_x$ is broken in Fig. S1(b). The Berry curvature for the first shell and up to the second shell are shown in Fig. S2(a) and (b), respectively.

B. First-shell approximation

We start by calculating the currents for the first shell, i.e., we set $\varepsilon_j = \varepsilon_1\delta_{j,1}$ and $\Omega_j = \Omega_1\delta_{j,1}$. In this case, the Bloch current can be written as

$$\boldsymbol{J}_{\text{Bloch}} = \frac{e}{V_c\hbar}\frac{\varepsilon_1 f_1^0}{2}\sum_{n=1}^{3}\left(\frac{i\boldsymbol{L}_n^{(1)}}{1-ie\tau\boldsymbol{E}\cdot\boldsymbol{L}_n^{(1)}/\hbar} - \frac{i\boldsymbol{L}_n^{(1)}}{1+ie\tau\boldsymbol{E}\cdot\boldsymbol{L}_n^{(1)}/\hbar}\right) = -\frac{e\varepsilon_1 f_1^0}{V_c\hbar}\sum_{n=1}^{3}\frac{\boldsymbol{L}_n^{(1)}(e\tau\boldsymbol{E}\cdot\boldsymbol{L}_n^{(1)}/\hbar)}{1+(e\tau\boldsymbol{E}\cdot\boldsymbol{L}_n^{(1)}/\hbar)^2}, \tag{48}$$

where f_1^0 is the Fourier component of the Fermi function for $\boldsymbol{R} = \pm\boldsymbol{L}_n^{(1)}$ $(n = 1, 2, 3)$ which are all real and equal due to $\mathcal{T}$ and $\mathcal{C}_{3z}$, respectively. Next, we introduce the dimensionless quantity

$$\omega_B\tau = e\tau EL/\hbar, \tag{49}$$

with ω_B the Bloch frequency and where $E = |\boldsymbol{E}|$. If we parameterize the electric field by an angle θ such that $\boldsymbol{E} = E\,(\cos\theta, \sin\theta)$, the component parallel to the field becomes

$$J^{\parallel}_{\text{Bloch}} \equiv \hat{E}\cdot\boldsymbol{J}_{\text{Bloch}} = -\frac{eL\varepsilon_1 f_1^0}{V_c\hbar}\sum_{n=1}^{3}\frac{\omega_B\tau(\hat{E}\cdot\boldsymbol{L}_n^{(1)}/L)^2}{1+(\omega_B\tau)^2(\hat{E}\cdot\boldsymbol{L}_n^{(1)}/L)^2} \tag{50}$$

$$= -\frac{eL\varepsilon_1 f_1^0}{V_c\hbar}\sum_{n=1}^{3}\frac{\omega_B\tau\cos^2\theta_n}{1+(\omega_B\tau)^2\cos^2\theta_n}, \tag{51}$$

where we defined the angles θ_n through

$$\hat{E}\cdot\boldsymbol{L}_n^{(1)} = L\cos\theta_n, \tag{52}$$

with $\theta_1 = \theta - \pi/3$, $\theta_2 = \theta + \pi$, and $\theta_3 = \theta + \pi/3$. This yields

$$J^{\parallel}_{\text{Bloch}}(\boldsymbol{E}) = -\frac{3eL\varepsilon_1 f_1^0}{V_c\hbar}F^{\parallel}_{\text{Bloch}}(\omega_B\tau,\theta), \qquad F^{\parallel}_{\text{Bloch}}(\zeta,\theta) = \zeta\,\frac{8+6\zeta^2+\zeta^4\cos^2(3\theta)}{16+24\zeta^2+9\zeta^4+\zeta^6\cos^2(3\theta)}. \tag{53}$$

Note that the filling of the band, as well as the effect of temperature, only enters via the overall factor f_1^0, which is plotted in Fig. S3. The function $F^{\parallel}_{\text{Bloch}}$ for fixed field strength as a function of θ is called a *rose curve*. It is shown in Fig. 2(b) of the main text. Because $F^{\parallel}_{\text{Bloch}}(\zeta,\theta)$ has no zeroes for finite ζ, the rose only has a single petal. We further find that $\max F^{\parallel}_{\text{Bloch}} \approx 0.3$ where the critical field is determined by a fifth-order polynomial in ζ^2. For $\theta = m\pi/3$ $(m \in \mathbb{Z})$ its real roots are $\zeta^2 = 2$ while for $\theta = \pi/6 + m\pi/3$ we find $\zeta^2 = 4/3$. This is shown in Fig. S4(a). If we

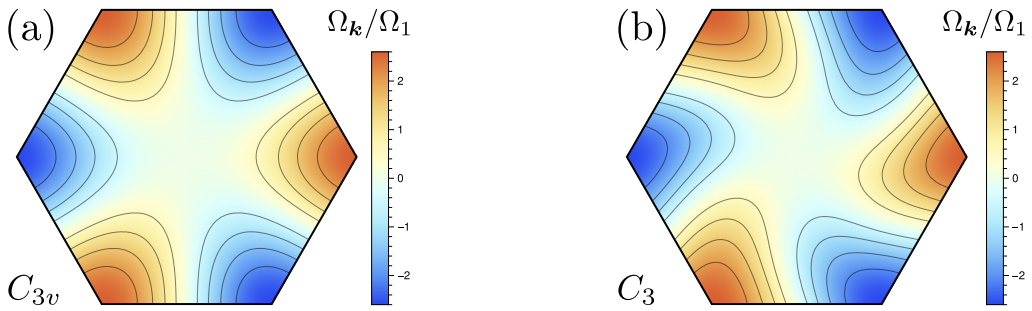

FIG. S2. Berry curvature for $\mathcal{C}_{3z}$ and $\mathcal{T}$ symmetry, but broken $\mathcal{C}_{2z}$ or inversion symmetry. (a) First-shell approximation. Only Ω_1 contributes and $\mathcal{M}_x$ is conserved. (b) Including the second shell breaks $\mathcal{M}_x$ symmetry, $\Omega_2/\Omega_1 = 0.2$.

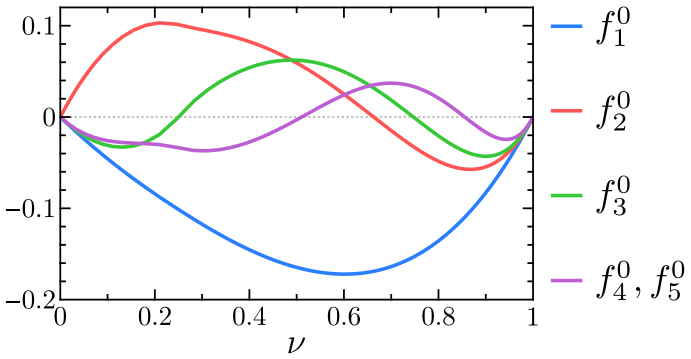

FIG. S3. Fourier components of the Fermi function for $\varepsilon_j = \varepsilon_1\delta_{j,1}$ and $k_BT/\varepsilon_1 = 0.01$ as a function of the filling ν.

define the direction perpendicular to the electric field as $\hat{E}\times\hat{z} = (\sin\theta, -\cos\theta)$, we find $(\hat{E}\times\hat{z})\cdot\boldsymbol{L}_n^{(1)} = L\sin\theta_n$ such that

$$J^{\perp}_{\text{Bloch}}(\boldsymbol{E}) \equiv (\hat{E}\times\hat{z})\cdot\boldsymbol{J}_{\text{Bloch}} = -\frac{eL\varepsilon_1 f_1^0}{V_c\hbar}\sum_{n=1}^{3}\frac{\omega_B\tau\sin\theta_n\cos\theta_n}{1+(\omega_B\tau)^2\cos^2\theta_n} = -\frac{3eL\varepsilon_1 f_1^0}{V_c\hbar}F^{\perp}_{\text{Bloch}}(\omega_B\tau,\theta), \tag{54}$$

with

$$F^{\perp}_{\text{Bloch}}(\zeta,\theta) = \frac{\zeta^5\sin(3\theta)\cos(3\theta)}{16+24\zeta^2+9\zeta^4+\zeta^6\cos^2(3\theta)}. \tag{55}$$

A polar plot of $|F^{\perp}_{\text{Bloch}}(\zeta,\theta)|$ is shown in Fig. 2(c) of the main text for different values of ζ. The transverse Bloch rose has twelve petals, since $F^{\perp}_{\text{Bloch}}$ vanishes for $\theta = m\pi/6$ ($m\in\mathbb{Z}$). Three of these angles correspond to the three mirror axes where the transverse response vanishes. The other three angles are a consequence of $\mathcal{T}$ in combination with mirror symmetry. Consider, for example, the case $E_y = 0$ (other axes are obtained by $\mathcal{C}_{3z}$). In this case, time-reversal symmetry dictates that the Bloch current is odd in E_x while mirror symmetry requires that the transverse component is even in E_x, and therefore $J^{\perp}_{\text{Bloch}}$ vanishes for $E_y = 0$. Summarized, we see that in the presence of time-reversal symmetry, the transverse Bloch current vanishes when the electric field is either parallel or perpendicular to a mirror axis. The extremal angles (tips of the petals) of $F^{\perp}_{\text{Bloch}}(\zeta,\theta)$ are shown as a function of ζ in Fig. S4(b).

For the geometric current, we have $\hat{E}\cdot\boldsymbol{J}_{\text{geom}} = 0$ and in the first-shell approximation,

$$J_{\text{geom}}(\boldsymbol{E}) \equiv (\hat{E}\times\hat{z})\cdot\boldsymbol{J}_{\text{geom}} = -\frac{e^2E}{V_c\hbar}\frac{\Omega_1 f_1^0}{2}\sum_{n=1}^{3}\left(\frac{i}{1-ie\tau\boldsymbol{E}\cdot\boldsymbol{L}_n^{(1)}/\hbar} - \frac{i}{1+ie\tau\boldsymbol{E}\cdot\boldsymbol{L}_n^{(1)}/\hbar}\right) \tag{56}$$

$$= \frac{e^2E}{V_c\hbar}\frac{\Omega_1 f_1^0}{2}\sum_{n=1}^{3}\frac{2e\tau\boldsymbol{E}\cdot\boldsymbol{L}_n^{(1)}/\hbar}{1+(e\tau\boldsymbol{E}\cdot\boldsymbol{L}_n^{(1)}/\hbar)^2} \tag{57}$$

$$= \frac{eL}{V_c\tau}\frac{\Omega_1 f_1^0}{L^2}\sum_{n=1}^{3}\frac{(\omega_B\tau)^2\cos\theta_n}{1+(\omega_B\tau)^2\cos^2\theta_n} = \frac{3eL}{V_c\tau}\frac{\Omega_1 f_1^0}{L^2}F_{\text{geom}}(\omega_B\tau,\theta), \tag{58}$$

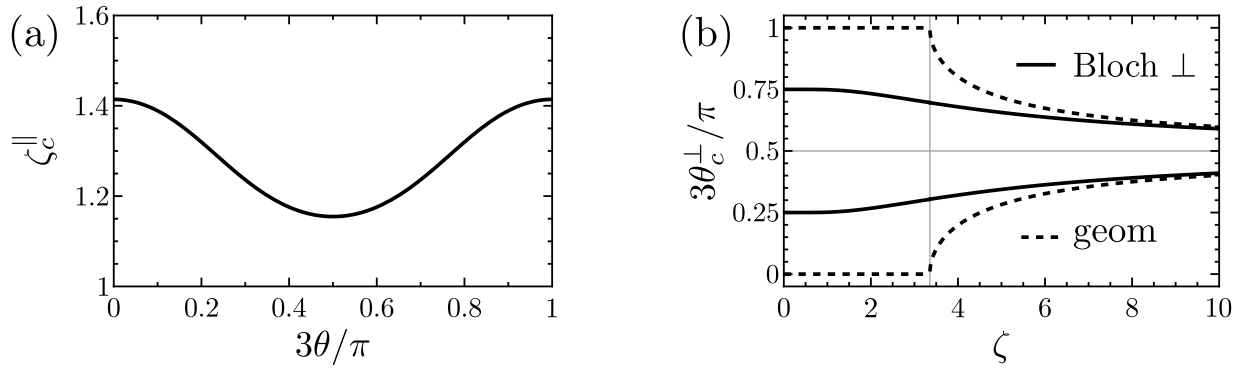

FIG. S4. (a) Critical field where $F^{\parallel}_{\mathrm{Bloch}}(\zeta,\theta)$ attains a maximum as a function of the field direction. (b) Critical angles where the absolute value of the transverse roses $F^{\perp}_{\mathrm{Bloch}}(\zeta,\theta)$ and $F_{\mathrm{geom}}(\zeta,\theta)$ reaches a maximum as a function of the field strength. Notice that the maxima both converge to $\theta=\pi/6$ for $\zeta\gg1$, for which the transverse roses vanish by $\mathcal{M}_x$ or $\mathcal{C}_{2y}$ symmetry.

with

$$F_{\mathrm{geom}}(\zeta,\theta)=\frac{\zeta^4\left(4+\zeta^2\right)\cos(3\theta)}{16+24\zeta^2+9\zeta^4+\zeta^6\cos^2(3\theta)}, \tag{59}$$

whose absolute value is shown in Fig. 2(d) of the main text. The geometric rose has six petals, since mirror symmetry precludes a transverse response when the electric field lies along a mirror axis. We find that minima of $|F_{\mathrm{geom}}(\zeta,\theta)|$ always occur at $\theta=m\pi/3$ and extrema occur for

$$\sin(6\theta)=0,\qquad \cos^2(3\theta)=\left(\frac{4+3\zeta^2}{\zeta^3}\right)^2, \tag{60}$$

such that the right-hand side has to be smaller or equal to one which yields $\zeta\geq3.355$ approximately. For $\zeta\gg1$, the maxima converge to $\theta=\pi/6+m\pi/3$. However, exactly at these angles, which correspond to mirror axes, the geometric current vanishes. The extremal angles of $F_{\mathrm{geom}}(\zeta,\theta)$ are shown in Fig. S4(b) as a function of ζ.

a. Weak-field limit The weak-field ($\zeta\ll1$) expansions are given by

$$F^{\parallel}_{\mathrm{Bloch}}(\zeta,\theta)\simeq\frac{\zeta}{2}-\frac{3\zeta^3}{8}+\frac{10+\cos(6\theta)}{32}\zeta^5, \tag{61}$$

$$F^{\perp}_{\mathrm{Bloch}}(\zeta,\theta)\simeq\frac{\sin(3\theta)\cos(3\theta)}{16}\zeta^5, \tag{62}$$

$$F_{\mathrm{geom}}(\zeta,\theta)\simeq\frac{\cos(3\theta)}{4}\zeta^4, \tag{63}$$

consistent with the symmetry analysis. The transverse Bloch current only appears at fifth order because the linear and cubic terms are forbidden by $\mathcal{C}_{3z}$. Indeed, for any in-plane vector $\boldsymbol{R}$, the longitudinal and transverse components of the Bloch current contain the sums

$$\sum_{n=1}^{3}(\hat{E}\cdot\mathcal{C}_{3z}^n\boldsymbol{R})^2=\frac{3}{2}|\boldsymbol{R}|^2, \tag{64}$$

$$\sum_{n=1}^{3}[(\hat{E}\times\hat{z})\cdot\mathcal{C}_{3z}^n\boldsymbol{R}](\hat{E}\cdot\mathcal{C}_{3z}^n\boldsymbol{R})=0, \tag{65}$$

such that the linear term in the transverse Bloch current is forbidden. Otherwise it would result in a symmetric part of the transverse linear conductivity. Similarly, for the cubic terms

$$\sum_{n=1}^{3}(\hat{E}\cdot\mathcal{C}_{3z}^n\boldsymbol{R})^4=\frac{9}{8}|\boldsymbol{R}|^4, \tag{66}$$

$$\sum_{n=1}^{3}[(\hat{E}\times\hat{z})\cdot\mathcal{C}_{3z}^n\boldsymbol{R}](\hat{E}\cdot\mathcal{C}_{3z}^n\boldsymbol{R})^3=0, \tag{67}$$

TABLE S2. Angles and scaling factors of the coordination shells of the triangular lattice, which are regular hexagons with radius L_j rotated by an angle θ_j relative to the first shell, shown here up to the seventh shell.

Shell	1	2	3	4	5	6	7
L_j/L	1	$\sqrt{3}$	2	$\sqrt{7}$	$\sqrt{7}$	3	$2\sqrt{3}$
θ_j	0	$\pi/6$	0	$\pi/6+\arctan\left(\sqrt{3}/5\right)$	$\pi/6-\arctan\left(\sqrt{3}/5\right)$	0	$\pi/6$

while all high-order terms are generally nonzero and depend on $\hat{E}$. We also note that the lowest-order geometric current is quartic in the field. The quadratic term, correspodning to the Berry curvature dipole, which is allowed by time-reversal symmetry, is proportional to

$$\hat{E}\cdot\sum_{\boldsymbol{R}}\boldsymbol{R}f^0_{\boldsymbol{R}}\Omega_{-\boldsymbol{R}}, \tag{68}$$

where

$$\sum_{\boldsymbol{R}}\boldsymbol{R}f^0_{\boldsymbol{R}}\Omega_{-\boldsymbol{R}}=\sum_{\boldsymbol{R}}\boldsymbol{R}f^0_{\mathcal{C}_{3z}\boldsymbol{R}}\Omega_{-\mathcal{C}_{3z}\boldsymbol{R}}=\mathcal{C}_{3z}^{-1}\sum_{\boldsymbol{R}}\boldsymbol{R}f^0_{\boldsymbol{R}}\Omega_{-\boldsymbol{R}}, \tag{69}$$

such that the vector sum vanishes. The cubic term involving the Berry curvature quadrupole, is forbidden by time-reversal symmetry. This is true for all odd powers:

$$(\hat{z}\times\boldsymbol{E})\sum_{\boldsymbol{R}}(\boldsymbol{E}\cdot\boldsymbol{R})^{2n}f^0_{\boldsymbol{R}}\Omega_{-\boldsymbol{R}}\propto\sum_{\boldsymbol{R}}(-\boldsymbol{E}\cdot\boldsymbol{R})^{2n}f^0_{-\boldsymbol{R}}\Omega_{\boldsymbol{R}}\overset{\mathcal{T}}{=}-\sum_{\boldsymbol{R}}(\boldsymbol{E}\cdot\boldsymbol{R})^{2n}f^0_{\boldsymbol{R}}\Omega_{-\boldsymbol{R}}. \tag{70}$$

b. Strong-field limit The strong-field ($\zeta\gg1$) expansions are given by

$$F^{\parallel}_{\mathrm{Bloch}}(\zeta,\theta)\simeq\frac{1}{\zeta}, \tag{71}$$

$$F^{\perp}_{\mathrm{Bloch}}(\zeta,\theta)\simeq\frac{\tan(3\theta)}{\zeta}, \tag{72}$$

$$F_{\mathrm{geom}}(\zeta,\theta)\simeq\frac{1}{\cos(3\theta)}, \tag{73}$$

where the last two lines hold only for $\theta\neq\pi/6+m\pi/3$. Precisely at these angles, the transverse currents vanish because of mirror symmetry, which is conserved if we only include the first shell.

C. General case including all shells

To obtain the general expression including contributions from all shells, we first note that all higher-order shells are obtained from the first shell by a rotation and a scaling. Hence, the results obtained for the first shell can be used to find the contribution of any shell. For example, the result for the second shell is obtained by sending

$$L\mapsto\sqrt{3}\,L, \tag{74}$$

$$\zeta\mapsto\sqrt{3}\,\zeta, \tag{75}$$

$$\theta\mapsto\theta+\frac{\pi}{6}, \tag{76}$$

in the first-shell expressions for $\boldsymbol{J}_{\mathrm{Bloch}}$ and $\boldsymbol{J}_{\mathrm{geom}}$. In this way, we find

$$J^{\parallel}_{\mathrm{Bloch}}(\boldsymbol{E})=-\frac{3eL}{V_c\hbar}\sum_j\frac{\varepsilon_j f^0_j L_j}{L}\,F^{\parallel}_{\mathrm{Bloch}}\left(\omega_B\tau L_j/L,\theta+\theta_j\right), \tag{77}$$

$$J^{\perp}_{\mathrm{Bloch}}(\boldsymbol{E})=-\frac{3eL}{V_c\hbar}\sum_j\frac{\varepsilon_j f^0_j L_j}{L}\,F^{\perp}_{\mathrm{Bloch}}\left(\omega_B\tau L_j/L,\theta+\theta_j\right), \tag{78}$$

$$J_{\mathrm{geom}}(\boldsymbol{E})=\frac{3eL}{V_c\tau}\sum_j\frac{\Omega_j f^0_j}{L^2}\frac{L}{L_j}\,F_{\mathrm{geom}}\left(\omega_B\tau L_j/L,\theta+\theta_j\right), \tag{79}$$

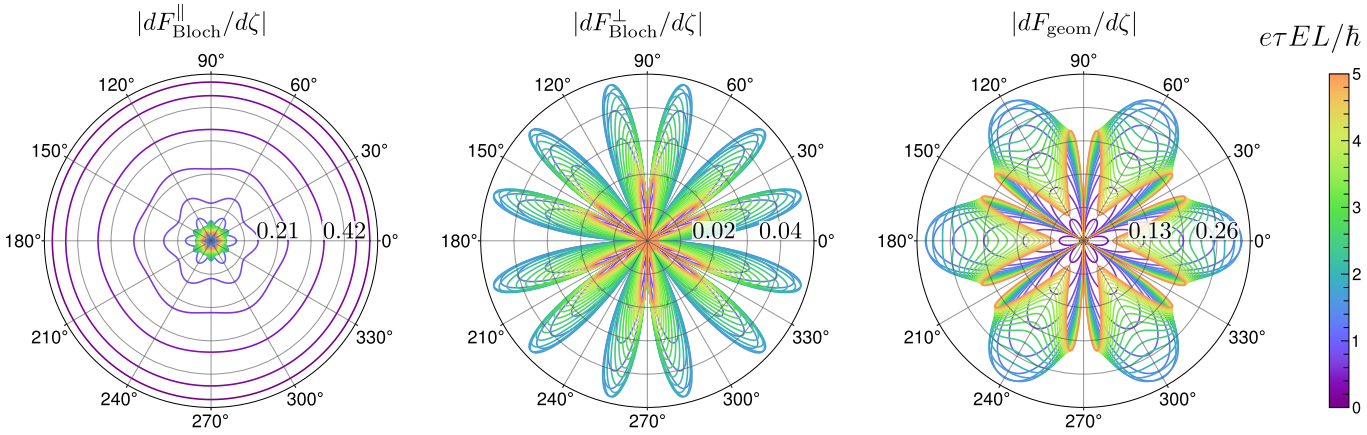

FIG. S5. Differential conductance roses for the first shell.

with $\omega_B = eEL/\hbar$ and where the sums run over shells. Here ε_j and Ω_j are the coefficients in the shell expansion of the band dispersion and the Berry curvature, respectively, and f^0_j are the corresponding Fourier components of the Fermi function. An overview of the angles and the scaling factors up to the seventh shell is shown in Table S2.

D. Differential conductance

We define the differential conductances as

$$\frac{dJ^{\parallel}_{\mathrm{Bloch}}}{dE} = -\frac{e^2\tau}{V_c\hbar^2}\sum_{\boldsymbol{R}}\frac{(\hat{E}\cdot\boldsymbol{R})^2 f^0_{\boldsymbol{R}}\varepsilon_{-\boldsymbol{R}}}{(1-ie\tau\boldsymbol{E}\cdot\boldsymbol{R}/\hbar)^2}, \tag{80}$$

$$\frac{dJ^{\perp}_{\mathrm{Bloch}}}{dE} = -\frac{e^2\tau}{V_c\hbar^2}\sum_{\boldsymbol{R}}\frac{[(\hat{E}\times\hat{z})\cdot\boldsymbol{R}](\hat{E}\cdot\boldsymbol{R}) f^0_{\boldsymbol{R}}\varepsilon_{-\boldsymbol{R}}}{(1-ie\tau\boldsymbol{E}\cdot\boldsymbol{R}/\hbar)^2}, \tag{81}$$

$$\frac{dJ_{\mathrm{geom}}}{dE} = -\frac{e^2}{V_c\hbar}\sum_{\boldsymbol{R}}\frac{f^0_{\boldsymbol{R}}\Omega_{-\boldsymbol{R}}}{(1-ie\tau\boldsymbol{E}\cdot\boldsymbol{R}/\hbar)^2}, \tag{82}$$

and thus

$$\frac{dJ^{\parallel}_{\mathrm{Bloch}}}{dE}(\boldsymbol{E}) = -\frac{3e^2\tau L^2}{V_c\hbar^2}\sum_j \frac{\varepsilon_j f^0_j L_j}{L}\left.\frac{dF^{\parallel}_{\mathrm{Bloch}}(\zeta L_j/L,\theta+\theta_j)}{d\zeta}\right|_{\zeta=\omega_B\tau}, \tag{83}$$

$$\frac{dJ^{\perp}_{\mathrm{Bloch}}}{dE}(\boldsymbol{E}) = -\frac{3e^2\tau L^2}{V_c\hbar^2}\sum_j \frac{\varepsilon_j f^0_j L_j}{L}\left.\frac{dF^{\perp}_{\mathrm{Bloch}}(\zeta L_j/L,\theta+\theta_j)}{d\zeta}\right|_{\zeta=\omega_B\tau}, \tag{84}$$

$$\frac{dJ_{\mathrm{geom}}}{dE}(\boldsymbol{E}) = \frac{3e^2L^2}{V_c\hbar}\sum_j \frac{\Omega_j f^0_j}{L^2}\frac{L}{L_j}\left.\frac{dF_{\mathrm{geom}}(\zeta L_j/L,\theta+\theta_j)}{d\zeta}\right|_{\zeta=\omega_B\tau}. \tag{85}$$

We show the differential conductance roses for the first shell in Fig. S5.

E. Summing contributions from two valleys

Finally, we consider two decoupled energy bands that are isolated from other bands with band dispersion $\varepsilon^{\nu}_{\boldsymbol{k}}$ and Berry curvature $\Omega^{\nu}_{\boldsymbol{k}}$, and that are related by time-reversal symmetry. Here, $\nu = \pm 1$ is the valley index. Time-reversal symmetry implies a relation between the energy bands and the Berry curvature of the two valleys:

$$\varepsilon^{\nu}_{\boldsymbol{k}} = \varepsilon^{-\nu}_{-\boldsymbol{k}}, \qquad \Omega^{\nu}_{\boldsymbol{k}} = -\Omega^{-\nu}_{-\boldsymbol{k}}. \tag{86}$$

Similarly in real space,

$$\varepsilon^{\nu}_{\boldsymbol{R}} = \varepsilon^{-\nu}_{-\boldsymbol{R}} = \left(\varepsilon^{-\nu}_{\boldsymbol{R}}\right)^*, \tag{87}$$

$$\Omega^{\nu}_{\boldsymbol{R}} = -\Omega^{-\nu}_{-\boldsymbol{R}} = -\left(\Omega^{-\nu}_{\boldsymbol{R}}\right)^*. \tag{88}$$

Let us consider the specific case where the symmetries of a single valley are given by the magnetic point group $3m' = \langle \mathcal{C}_{3z}, \mathcal{M}_x\mathcal{T}\rangle$. As before, we expand the energy bands in terms of the coordination shells:

$$\varepsilon^{\nu}_{\boldsymbol{k}} = \varepsilon_0 + \varepsilon_1 \sum_{n=1}^{3} \cos(\boldsymbol{k}\cdot\boldsymbol{L}^{(1)}_n + \nu\phi) + \cdots, \tag{89}$$

$$\Omega^{\nu}_{\boldsymbol{k}} = \nu\Omega_0 + \Omega_1 \sum_{n=1}^{3} \sin(\boldsymbol{k}\cdot\boldsymbol{L}^{(1)}_n + \nu\xi) + \cdots. \tag{90}$$

where ϕ and ξ are phases that are allowed because $\mathcal{T}$ is broken within a single valley. Using the relations between the real-space Fourier components of different valleys, the total current can be written solely in terms of quantities at a single valley,

$$\boldsymbol{J}_{\text{Bloch}} = \frac{2e}{V_c\hbar} \sum_{\boldsymbol{R}} \frac{i\boldsymbol{R}\,\text{Re}\left(f^{0+}_{\boldsymbol{R}}\varepsilon^{+}_{-\boldsymbol{R}}\right)}{1 - ie\tau\boldsymbol{E}\cdot\boldsymbol{R}/\hbar}, \tag{91}$$

$$\boldsymbol{J}_{\text{geom}} = (\hat{z}\times\boldsymbol{E})\,\frac{2e^2}{V_c\hbar} \sum_{\boldsymbol{R}} \frac{i\text{Im}\left(f^{0+}_{\boldsymbol{R}}\Omega^{+}_{-\boldsymbol{R}}\right)}{1 - ie\tau\boldsymbol{E}\cdot\boldsymbol{R}/\hbar}. \tag{92}$$

In the first-shell approximation, we find

$$\boldsymbol{J}_{\text{Bloch}}(\boldsymbol{E}) = -\frac{6eL\varepsilon_1|f^0_1|\cos(\chi-\phi)}{V_c\hbar}\left[\hat{E}F^{\parallel}_{\text{Bloch}}(\omega_B\tau,\theta) + (\hat{E}\times\hat{z})\,F^{\perp}_{\text{Bloch}}(\omega_B\tau,\theta)\right], \tag{93}$$

$$\boldsymbol{J}_{\text{geom}}(\boldsymbol{E}) = (\hat{E}\times\hat{z})\,\frac{6eL}{V_c\tau}\frac{\Omega_1|f^0_1|\cos(\chi-\xi)}{L^2}\,F_{\text{geom}}(\omega_B\tau,\theta), \tag{94}$$

where $f^{0\nu}_{\pm\boldsymbol{R}} = |f^0_1|e^{\pm i\nu\chi}$ for $\boldsymbol{R} = \boldsymbol{L}^{(1)}_n$ $(n = 1, 2, 3)$.

III. PERIODICALLY-BUCKLED GRAPHENE

A. Strain profile from height modulation

Given a height modulation of the monolayer graphene, induced by a buckling transition, we want to obtain the corresponding strain tensor. The strain tensor u_{ij} $(i, j = x, y)$ is defined [5] by considering the change in length between two points with initial (infinitesimal and in-plane) separation dr_i after a deformation: $\left[(dr_i + du_i)^2 + dh^2\right] - dr_i^2 \equiv 2u_{ij}dr_idr_j$. Up to lowest order in the displacements, the strain tensor is given by

$$u_{ij}(\boldsymbol{r}) = \frac{1}{2}\left[\partial_i u_j + \partial_j u_i + (\partial_i h)\,(\partial_j h)\right], \tag{95}$$

with $\partial_i = \partial/\partial r_i$ and where $u_i(\boldsymbol{r})$ and $h(\boldsymbol{r})$ are the in-plane and out-of-plane displacements, respectively.

If the displacements are periodic, we can write them as a Fourier series:

$$u_i(\boldsymbol{r}) = \sum_{\boldsymbol{\mathcal{G}}} u_{i\boldsymbol{\mathcal{G}}}\, e^{i\boldsymbol{\mathcal{G}}\cdot\boldsymbol{r}}, \tag{96}$$

$$h(\boldsymbol{r}) = \sum_{\boldsymbol{\mathcal{G}}} h_{\boldsymbol{\mathcal{G}}}\, e^{i\boldsymbol{\mathcal{G}}\cdot\boldsymbol{r}}, \tag{97}$$

where $\boldsymbol{\mathcal{G}}$ is a reciprocal lattice vector of the periodic modulation (not of the monolayer graphene) and $u_{i\boldsymbol{0}} = h_{\boldsymbol{0}} = 0$. For later convenience, we also define

$$f_{ij}(\boldsymbol{r}) \equiv [\partial_i h(\boldsymbol{r})]\,[\partial_j h(\boldsymbol{r})] = \sum_{\boldsymbol{\mathcal{G}}} f_{ij\boldsymbol{\mathcal{G}}}\, e^{i\boldsymbol{\mathcal{G}}\cdot\boldsymbol{r}}, \tag{98}$$

where

$$f_{ij\boldsymbol{\mathcal{G}}} = -\sum_{\boldsymbol{\mathcal{G}}'} h_{\boldsymbol{\mathcal{G}}'} h_{\boldsymbol{\mathcal{G}}-\boldsymbol{\mathcal{G}}'} \mathcal{G}'_i \left(\mathcal{G}_j - \mathcal{G}'_j\right). \tag{99}$$

The strain tensor becomes

$$u_{ij}(\boldsymbol{r}) = \frac{1}{2}\sum_{\boldsymbol{\mathcal{G}}} \left[i\left(\mathcal{G}_i u_{j\boldsymbol{\mathcal{G}}} + \mathcal{G}_j u_{i\boldsymbol{\mathcal{G}}}\right) + f_{ij\boldsymbol{\mathcal{G}}}\right] e^{i\boldsymbol{\mathcal{G}}\cdot\boldsymbol{r}}. \tag{100}$$

A fixed height profile $h(\boldsymbol{r})$ will give rise to in-plane displacements as the graphene lattice relaxes. The in-plane displacements can be found by minimizing the elastic energy density [6, 7]:

$$\mathcal{E}_{\text{elas}} = \frac{1}{V}\int d^2\boldsymbol{r}\left[\frac{\lambda}{2}\left(u_{xx}+u_{yy}\right)^2 + \mu\left(u_{xx}^2 + u_{yy}^2 + 2u_{xy}^2\right)\right] \tag{101}$$

$$= \frac{1}{V}\int d^2\boldsymbol{r}\left[\left(\frac{\lambda}{2}+\mu\right)\left(u_{xx}^2+u_{yy}^2\right) + \lambda u_{xx}u_{yy} + 2\mu u_{xy}^2\right], \tag{102}$$

where λ and μ are the Lamé parameters for graphene. Plugging in the Fourier expansions, we obtain

$$\frac{1}{V}\int d^2\boldsymbol{r}\, u_{ii}^2 = \frac{1}{V}\sum_{\boldsymbol{\mathcal{G}},\boldsymbol{\mathcal{G}}'}\int d^2\boldsymbol{r}\left(i\mathcal{G}_i u_{i\boldsymbol{\mathcal{G}}} + \frac{f_{ii\boldsymbol{\mathcal{G}}}}{2}\right)\left(i\mathcal{G}'_i u_{i\boldsymbol{\mathcal{G}}'} + \frac{f_{ii\boldsymbol{\mathcal{G}}'}}{2}\right) e^{i(\boldsymbol{\mathcal{G}}+\boldsymbol{\mathcal{G}}')\cdot\boldsymbol{r}} \tag{103}$$

$$= \sum_{\boldsymbol{\mathcal{G}}}\left|i\mathcal{G}_i u_{i\boldsymbol{\mathcal{G}}} + \frac{f_{ii\boldsymbol{\mathcal{G}}}}{2}\right|^2, \tag{104}$$

$$\frac{1}{V}\int d^2\boldsymbol{r}\, u_{xx}u_{yy} = \sum_{\boldsymbol{\mathcal{G}}}\left(i\mathcal{G}_x u_{x\boldsymbol{\mathcal{G}}} + \frac{f_{xx\boldsymbol{\mathcal{G}}}}{2}\right)\left(-i\mathcal{G}_y u^*_{y\boldsymbol{\mathcal{G}}} + \frac{f^*_{yy\boldsymbol{\mathcal{G}}}}{2}\right) \tag{105}$$

$$= \frac{1}{2}\sum_{\boldsymbol{\mathcal{G}}}\left[\left(i\mathcal{G}_x u_{x\boldsymbol{\mathcal{G}}} + \frac{f_{xx\boldsymbol{\mathcal{G}}}}{2}\right)\left(-i\mathcal{G}_y u^*_{y\boldsymbol{\mathcal{G}}} + \frac{f^*_{yy\boldsymbol{\mathcal{G}}}}{2}\right) + \text{c.c.}\right], \tag{106}$$

$$\frac{1}{V}\int d^2\boldsymbol{r}\, u_{xy}^2 = \frac{1}{4}\sum_{\boldsymbol{\mathcal{G}}}\left(i\mathcal{G}_x u_{y\boldsymbol{\mathcal{G}}} + i\mathcal{G}_y u_{x\boldsymbol{\mathcal{G}}} + f_{xy\boldsymbol{\mathcal{G}}}\right)\left(-i\mathcal{G}_x u^*_{y\boldsymbol{\mathcal{G}}} - i\mathcal{G}_y u^*_{x\boldsymbol{\mathcal{G}}} + f^*_{xy\boldsymbol{\mathcal{G}}}\right). \tag{107}$$

Hence, the elastic energy density becomes

$$\mathcal{E}_{\text{elas}} = \left(\frac{\lambda}{2}+\mu\right)\sum_{\boldsymbol{\mathcal{G}}}\left(i\mathcal{G}_x u_{x\boldsymbol{\mathcal{G}}} + \frac{f_{xx\boldsymbol{\mathcal{G}}}}{2}\right)\left(-i\mathcal{G}_x u^*_{x\boldsymbol{\mathcal{G}}} + \frac{f^*_{xx\boldsymbol{\mathcal{G}}}}{2}\right) \tag{108}$$

$$+ \left(\frac{\lambda}{2}+\mu\right)\sum_{\boldsymbol{\mathcal{G}}}\left(i\mathcal{G}_y u_{y\boldsymbol{\mathcal{G}}} + \frac{f_{yy\boldsymbol{\mathcal{G}}}}{2}\right)\left(-i\mathcal{G}_y u^*_{y\boldsymbol{\mathcal{G}}} + \frac{f^*_{yy\boldsymbol{\mathcal{G}}}}{2}\right) \tag{109}$$

$$+ \frac{\lambda}{2}\sum_{\boldsymbol{\mathcal{G}}}\left[\left(i\mathcal{G}_x u_{x\boldsymbol{\mathcal{G}}} + \frac{f_{xx\boldsymbol{\mathcal{G}}}}{2}\right)\left(-i\mathcal{G}_y u^*_{y\boldsymbol{\mathcal{G}}} + \frac{f^*_{yy\boldsymbol{\mathcal{G}}}}{2}\right) + \text{c.c.}\right] \tag{110}$$

$$+ \frac{\mu}{2}\sum_{\boldsymbol{\mathcal{G}}}\left(i\mathcal{G}_x u_{y\boldsymbol{\mathcal{G}}} + i\mathcal{G}_y u_{x\boldsymbol{\mathcal{G}}} + f_{xy\boldsymbol{\mathcal{G}}}\right)\left(-i\mathcal{G}_x u^*_{y\boldsymbol{\mathcal{G}}} - i\mathcal{G}_y u^*_{x\boldsymbol{\mathcal{G}}} + f^*_{xy\boldsymbol{\mathcal{G}}}\right). \tag{111}$$

By extremizing the elastic energy with respect to $u^*_{i\boldsymbol{\mathcal{G}}}$ we obtain equations for the Fourier components $u_{i\boldsymbol{\mathcal{G}}}$ in terms of $f_{ij\boldsymbol{\mathcal{G}}}$ (and thus $h_{i\boldsymbol{\mathcal{G}}}$). We find

$$\frac{\partial\mathcal{E}}{\partial u^*_{x\boldsymbol{\mathcal{G}}}} = -i\mathcal{G}_x\left[\left(\frac{\lambda}{2}+\mu\right)\left(i\mathcal{G}_x u_{x\boldsymbol{\mathcal{G}}} + \frac{f_{xx\boldsymbol{\mathcal{G}}}}{2}\right) + \frac{\lambda}{2}\left(i\mathcal{G}_y u_{y\boldsymbol{\mathcal{G}}} + \frac{f_{yy\boldsymbol{\mathcal{G}}}}{2}\right)\right] - i\mathcal{G}_y\frac{\mu}{2}\left(i\mathcal{G}_x u_{y\boldsymbol{\mathcal{G}}} + i\mathcal{G}_y u_{x\boldsymbol{\mathcal{G}}} + f_{xy\boldsymbol{\mathcal{G}}}\right), \tag{112}$$

$$\frac{\partial\mathcal{E}}{\partial u^*_{y\boldsymbol{\mathcal{G}}}} = -i\mathcal{G}_y\left[\left(\frac{\lambda}{2}+\mu\right)\left(i\mathcal{G}_y u_{y\boldsymbol{\mathcal{G}}} + \frac{f_{yy\boldsymbol{\mathcal{G}}}}{2}\right) + \frac{\lambda}{2}\left(i\mathcal{G}_x u_{x\boldsymbol{\mathcal{G}}} + \frac{f_{xx\boldsymbol{\mathcal{G}}}}{2}\right)\right] - i\mathcal{G}_x\frac{\mu}{2}\left(i\mathcal{G}_x u_{y\boldsymbol{\mathcal{G}}} + i\mathcal{G}_y u_{x\boldsymbol{\mathcal{G}}} + f_{xy\boldsymbol{\mathcal{G}}}\right). \tag{113}$$

Setting the above two equations equal to zero, yields solutions

$$u_{x\boldsymbol{\mathcal{G}}} = \frac{i}{2\left(\lambda+2\mu\right)|\boldsymbol{\mathcal{G}}|^4}\left\{f^{\boldsymbol{\mathcal{G}}}_{xx}\mathcal{G}_x\left[\mathcal{G}_x^2\left(\lambda+2\mu\right)+\mathcal{G}_y^2\left(3\lambda+4\mu\right)\right] + \left(f^{\boldsymbol{\mathcal{G}}}_{yy}\mathcal{G}_x - 2f^{\boldsymbol{\mathcal{G}}}_{xy}\mathcal{G}_y\right)\left[\mathcal{G}_x^2\lambda - \mathcal{G}_y^2\left(\lambda+2\mu\right)\right]\right\}, \tag{114}$$

$$u_{y\boldsymbol{\mathcal{G}}} = \frac{i}{2\left(\lambda+2\mu\right)|\boldsymbol{\mathcal{G}}|^4}\left\{f^{\boldsymbol{\mathcal{G}}}_{yy}\mathcal{G}_y\left[\mathcal{G}_y^2\left(\lambda+2\mu\right)+\mathcal{G}_x^2\left(3\lambda+4\mu\right)\right] + \left(f^{\boldsymbol{\mathcal{G}}}_{xx}\mathcal{G}_y - 2f^{\boldsymbol{\mathcal{G}}}_{xy}\mathcal{G}_x\right)\left[\mathcal{G}_y^2\lambda - \mathcal{G}_x^2\left(\lambda+2\mu\right)\right]\right\}. \tag{115}$$

1. Pseudomagnetic field

Shear strain breaks the microscopic $\mathcal{C}_{3z}$ symmetry and couples to the low-energy Dirac electrons of graphene through a pseudo vector potential $\nu\boldsymbol{\mathcal{A}}(\boldsymbol{r})$ with $\nu = \pm 1$ the valley index and [8–12]

$$\boldsymbol{\mathcal{A}} = -\frac{\sqrt{3}\hbar\beta}{2ea}\begin{pmatrix} u_{xx} - u_{yy} \\ -2u_{xy} \end{pmatrix}, \tag{116}$$

where $e > 0$ is the elementary charge, $a \approx 0.246$ nm is the lattice constant of graphene, and $\beta \sim 1$ is the electron Grüneisen parameter for graphene. By using the results given above, we find that

$$u^{\boldsymbol{\mathcal{G}}}_{xx} - u^{\boldsymbol{\mathcal{G}}}_{yy} = \frac{(\lambda+\mu)\left(\mathcal{G}_y^2 - \mathcal{G}_x^2\right)\left(\mathcal{G}_x^2 f^{\boldsymbol{\mathcal{G}}}_{yy} - 2\mathcal{G}_x\mathcal{G}_y f^{\boldsymbol{\mathcal{G}}}_{xy} + \mathcal{G}_y^2 f^{\boldsymbol{\mathcal{G}}}_{xx}\right)}{(\lambda+2\mu)\,|\boldsymbol{\mathcal{G}}|^4}, \tag{117}$$

$$-2u^{\boldsymbol{\mathcal{G}}}_{xy} = \frac{2(\lambda+\mu)\,\mathcal{G}_x\mathcal{G}_y\left(\mathcal{G}_x^2 f^{\boldsymbol{\mathcal{G}}}_{yy} - 2\mathcal{G}_x\mathcal{G}_y f^{\boldsymbol{\mathcal{G}}}_{xy} + \mathcal{G}_y^2 f^{\boldsymbol{\mathcal{G}}}_{xx}\right)}{(\lambda+2\mu)\,|\boldsymbol{\mathcal{G}}|^4}, \tag{118}$$

such that

$$\boldsymbol{\mathcal{A}}(\boldsymbol{r}) = \frac{\sqrt{3}\hbar\beta}{2ea}\frac{\lambda+\mu}{\lambda+2\mu}\sum_{\boldsymbol{\mathcal{G}}}\frac{\mathcal{G}_x^2 f^{\boldsymbol{\mathcal{G}}}_{yy} - 2\mathcal{G}_x\mathcal{G}_y f^{\boldsymbol{\mathcal{G}}}_{xy} + \mathcal{G}_y^2 f^{\boldsymbol{\mathcal{G}}}_{xx}}{|\boldsymbol{\mathcal{G}}|^4}\begin{pmatrix} \mathcal{G}_x^2 - \mathcal{G}_y^2 \\ -2\mathcal{G}_x\mathcal{G}_y \end{pmatrix} e^{i\boldsymbol{\mathcal{G}}\cdot\boldsymbol{r}}. \tag{119}$$

Likewise, the pseudomagnetic field $\boldsymbol{\mathcal{B}}(\boldsymbol{r}) = \mathcal{B}(\boldsymbol{r})\hat{z}$ becomes

$$\mathcal{B}(\boldsymbol{r}) = \partial_x\mathcal{A}_y - \partial_y\mathcal{A}_x = \frac{\sqrt{3}\hbar\beta}{2ea}\frac{\lambda+\mu}{\lambda+2\mu}\sum_{\boldsymbol{\mathcal{G}}}\frac{i\mathcal{G}_y\left(\mathcal{G}_y^2 - 3\mathcal{G}_x^2\right)\left(\mathcal{G}_x^2 f^{\boldsymbol{\mathcal{G}}}_{yy} - 2\mathcal{G}_x\mathcal{G}_y f^{\boldsymbol{\mathcal{G}}}_{xy} + \mathcal{G}_y^2 f^{\boldsymbol{\mathcal{G}}}_{xx}\right)}{|\boldsymbol{\mathcal{G}}|^4} e^{i\boldsymbol{\mathcal{G}}\cdot\boldsymbol{r}}. \tag{120}$$

Notice that $\boldsymbol{\mathcal{G}} = \boldsymbol{0}$ does not contribute (i.e., there is no net flux) since the nominator scales as $|\boldsymbol{\mathcal{G}}|^5$.

2. Triangular height profile

We now consider a height profile that conserves $\mathcal{C}_{3z}$ symmetry in the first-star approximation,

$$h(\boldsymbol{r}) = h_0\sum_{n=1}^{3}\cos\left(\boldsymbol{\mathcal{G}}_n\cdot\boldsymbol{r} + \frac{\pi}{4} + \phi\right), \tag{121}$$

where ϕ is a parameter that controls the shape of the height profile. Note that while ϕ cannot be absorbed in a coordinate shift, Eq. (121) is invariant under $\phi \mapsto \phi + 2\pi/3$ up to an overall translation. The finite Fourier components are $h_{\pm\boldsymbol{\mathcal{G}}_n} = h_0 e^{\pm i(\phi+\pi/4)}/2$ $(n = 1, 2, 3)$ and where

$$\boldsymbol{\mathcal{G}}_1 = \frac{4\pi}{\sqrt{3}L}\begin{pmatrix} 0 \\ 1 \end{pmatrix}, \qquad \boldsymbol{\mathcal{G}}_{2/3} = \frac{4\pi}{\sqrt{3}L}\begin{pmatrix} \mp\sqrt{3}/2 \\ -1/2 \end{pmatrix}, \tag{122}$$

with $\boldsymbol{\mathcal{G}}_3 = -\boldsymbol{\mathcal{G}}_1 - \boldsymbol{\mathcal{G}}_2$ and L the lattice constant of the height modulation. These are the three shortest nonzero reciprocal lattice vectors that are related by $\mathcal{C}_{3z}$ symmetry. We calculate all the Fourier components of $f_{ij}(\boldsymbol{r})$ with Mathematica. We then find that

$$\begin{aligned} &\frac{i\mathcal{G}_y\left(\mathcal{G}_y^2 - 3\mathcal{G}_x^2\right)\left(\mathcal{G}_x^2 f^{\boldsymbol{\mathcal{G}}}_{yy} - 2\mathcal{G}_x\mathcal{G}_y f^{\boldsymbol{\mathcal{G}}}_{xy} + \mathcal{G}_y^2 f^{\boldsymbol{\mathcal{G}}}_{xx}\right)}{|\boldsymbol{\mathcal{G}}|^4} \\ &= \frac{3\mathcal{G}^3 h_0^2}{8}\left[e^{-2i\phi}\left(\delta_{\boldsymbol{\mathcal{G}},\boldsymbol{\mathcal{G}}_1} + \delta_{\boldsymbol{\mathcal{G}},\boldsymbol{\mathcal{G}}_2} + \delta_{\boldsymbol{\mathcal{G}},\boldsymbol{\mathcal{G}}_3}\right) + e^{2i\phi}\left(\delta_{\boldsymbol{\mathcal{G}},-\boldsymbol{\mathcal{G}}_1} + \delta_{\boldsymbol{\mathcal{G}},-\boldsymbol{\mathcal{G}}_2} + \delta_{\boldsymbol{\mathcal{G}},-\boldsymbol{\mathcal{G}}_3}\right)\right], \end{aligned} \tag{123}$$

with $\mathcal{G} = 4\pi/\sqrt{3}L$ and therefore

$$\mathcal{B}(\boldsymbol{r}) = \mathcal{B}_0\sum_{n=1}^{3}\cos\left(\boldsymbol{\mathcal{G}}_n\cdot\boldsymbol{r} - 2\phi\right), \qquad \mathcal{B}_0 = \frac{\hbar\beta}{ea}\frac{\lambda+\mu}{\lambda+2\mu}\frac{8\pi^3 h_0^2}{L^3}. \tag{124}$$

We find that the pseudomagnetic field is invariant under $\phi \mapsto \phi + \pi/3$ up to an overall translation, which changes the sign of the height profile. Hence we can restrict ourselves to $\phi \in (-\pi/6, \pi/6]$. The pseudomagnetic field has $\mathcal{C}_{6z}$ symmetry for the special case $\phi = \pi/12$.

3. Rectangular height profile

Let us also consider a height profile that conserves $\mathcal{C}_{4z}$ symmetry in the first-star approximation,

$$h(\boldsymbol{r}) = h_0 \sum_{n=1}^{2} \cos\left(\boldsymbol{\mathcal{G}}_n \cdot \boldsymbol{r}\right). \tag{125}$$

In this case, a phase factor can always be absorbed in a coordinate shift since there are only two reciprocal lattice vectors. The finite Fourier components are now given by $h_{\pm\boldsymbol{\mathcal{G}}_n} = h_0/2$ $(n = 1, 2)$ where

$$\boldsymbol{\mathcal{G}}_1 = \frac{2\pi}{L}\begin{pmatrix}1\\0\end{pmatrix}, \qquad \boldsymbol{\mathcal{G}}_2 = \frac{2\pi}{L}\begin{pmatrix}0\\1\end{pmatrix}. \tag{126}$$

We calculate all the Fourier components of $f_{ij}(\boldsymbol{r})$ with Mathematica and find

$$\begin{aligned}&\frac{i\mathcal{G}_y\left(\mathcal{G}_y^2 - 3\mathcal{G}_x^2\right)\left(\mathcal{G}_x^2 f_{yy}^{\boldsymbol{\mathcal{G}}} - 2\mathcal{G}_x\mathcal{G}_y f_{xy}^{\boldsymbol{\mathcal{G}}} + \mathcal{G}_y^2 f_{xx}^{\boldsymbol{\mathcal{G}}}\right)}{|\boldsymbol{\mathcal{G}}|^4}\\ &= \frac{\mathcal{G}^3 h_0^2}{4i}\left[\left(\delta_{\boldsymbol{\mathcal{G}},\boldsymbol{\mathcal{G}}_2+\boldsymbol{\mathcal{G}}_1} + \delta_{\boldsymbol{\mathcal{G}},\boldsymbol{\mathcal{G}}_2-\boldsymbol{\mathcal{G}}_1}\right) - \left(\delta_{\boldsymbol{\mathcal{G}},-\boldsymbol{\mathcal{G}}_2-\boldsymbol{\mathcal{G}}_1} + \delta_{\boldsymbol{\mathcal{G}},-\boldsymbol{\mathcal{G}}_2+\boldsymbol{\mathcal{G}}_1}\right)\right],\end{aligned} \tag{127}$$

with $\mathcal{G} = 2\pi/L$ and

$$\mathcal{B}(\boldsymbol{r}) = \mathcal{B}_0\left(\sin\left[\left(\boldsymbol{\mathcal{G}}_2 + \boldsymbol{\mathcal{G}}_1\right)\cdot\boldsymbol{r}\right] + \sin\left[\left(\boldsymbol{\mathcal{G}}_2 - \boldsymbol{\mathcal{G}}_1\right)\cdot\boldsymbol{r}\right]\right), \qquad \mathcal{B}_0 = \frac{\hbar\beta}{ea}\frac{\lambda+\mu}{\lambda+2\mu}\frac{2\sqrt{3}\pi^3 h_0^2}{L^3}. \tag{128}$$

Under $\mathcal{C}_{2z}$, the pseudomagnetic field picks up an extra sign because the valleys are interchanged. Hence the pseudomagnetic field for a height profile with $\mathcal{C}_{4z}$ symmetry always has $\mathcal{C}_{2z}$ symmetry, as expected. In this case, band crossings between backfolded bands are protected locally in momentum space by $\mathcal{C}_{2z}\mathcal{T}$ symmetry.

B. Continuum model

When the height profile varies slowly compared to the graphene lattice constant, i.e., $L \gg a$, we can use the valley-projected continuum theory [7, 13],

$$\hat{H}_\nu = \int d^2\boldsymbol{r}\, \hat{\psi}_\nu^\dagger(\boldsymbol{r})\left\{\hbar v\left[-i\nabla + \frac{\nu e}{\hbar}\boldsymbol{\mathcal{A}}(\boldsymbol{r})\right]\cdot(\nu\sigma_x, \sigma_y) + \mathcal{V}(\boldsymbol{r})\sigma_0\right\}\hat{\psi}_\nu(\boldsymbol{r}), \tag{129}$$

where σ_x and σ_y are Pauli matrices, σ_0 is the 2×2 identity matrix, $\hat{\psi}_\nu = (\hat{\psi}_{\nu A}, \hat{\psi}_{\nu B})^t$ are field operators satisfying $\{\hat{\psi}_\nu^\dagger(\boldsymbol{r}), \hat{\psi}_{\nu'}(\boldsymbol{r}')\} = \delta_{\nu\nu'}\delta^{(2)}(\boldsymbol{r}-\boldsymbol{r}')$, and we take $\hbar v \approx 575.2$ meV nm [14]. The pseudo vector potential and scalar potential are given in terms of their Fourier series,

$$\boldsymbol{\mathcal{A}}(\boldsymbol{r}) = \sum_{\boldsymbol{\mathcal{G}}} \boldsymbol{\mathcal{A}}_{\boldsymbol{\mathcal{G}}}\, e^{i\boldsymbol{\mathcal{G}}\cdot\boldsymbol{r}}, \qquad \mathcal{V}(\boldsymbol{r}) = \mathcal{V}_0\frac{h(\boldsymbol{r})}{h_0} = \sum_{\boldsymbol{\mathcal{G}}}\mathcal{V}_{\boldsymbol{\mathcal{G}}}\, e^{i\boldsymbol{\mathcal{G}}\cdot\boldsymbol{r}}. \tag{130}$$

The Hamiltonian can be diagonalized by Fourier transformation,

$$\hat{\psi}_\nu(\boldsymbol{r}) = \frac{1}{\sqrt{V}}\sum_{\boldsymbol{k}}\sum_{\boldsymbol{\mathcal{G}}} e^{i(\boldsymbol{k}-\boldsymbol{\mathcal{G}})\cdot\boldsymbol{r}}\hat{c}_{\nu,\boldsymbol{k}-\boldsymbol{\mathcal{G}}}, \tag{131}$$

where the sum over $\boldsymbol{k}$ is restricted to the first superlattice Brillouin zone (SBZ) and $\{\hat{c}_{\nu,\boldsymbol{k}-\boldsymbol{\mathcal{G}}}, \hat{c}_{\nu,\boldsymbol{k}'-\boldsymbol{\mathcal{G}}'}\} = \delta_{\boldsymbol{k},\boldsymbol{k}'}\delta_{\boldsymbol{\mathcal{G}},\boldsymbol{\mathcal{G}}'}$. Note that every wave vector has a unique decomposition as $\boldsymbol{k}-\boldsymbol{\mathcal{G}}$. The Hamiltonian becomes

$$\hat{H}_\nu = \frac{1}{V}\sum_{\boldsymbol{k},\boldsymbol{k}'}\sum_{\boldsymbol{\mathcal{G}},\boldsymbol{\mathcal{G}}'}\int d^2\boldsymbol{r}\,\hat{c}^\dagger_{\nu,\boldsymbol{k}'-\boldsymbol{\mathcal{G}}'}e^{-i(\boldsymbol{k}'-\boldsymbol{\mathcal{G}}')\cdot\boldsymbol{r}}\left\{\hbar v\left[\boldsymbol{k}-\boldsymbol{\mathcal{G}}+\frac{\nu e}{\hbar}\boldsymbol{\mathcal{A}}(\boldsymbol{r})\right]\cdot(\nu\sigma_x,\sigma_y) + \mathcal{V}(\boldsymbol{r})\right\}e^{i(\boldsymbol{k}-\boldsymbol{\mathcal{G}})\cdot\boldsymbol{r}}\hat{c}_{\nu,\boldsymbol{k}-\boldsymbol{\mathcal{G}}}. \tag{132}$$

Next, we note that

$$\frac{1}{V}\int d^2\boldsymbol{r}\, e^{-i(\boldsymbol{k}'-\boldsymbol{\mathcal{G}}')\cdot\boldsymbol{r}}\, e^{i(\boldsymbol{k}-\boldsymbol{\mathcal{G}})\cdot\boldsymbol{r}} = \delta_{\boldsymbol{k}\boldsymbol{k}'}\delta_{\boldsymbol{\mathcal{G}}\boldsymbol{\mathcal{G}}'}, \tag{133}$$

$$\frac{1}{V}\int d^2\boldsymbol{r}\, e^{-i(\boldsymbol{k}'-\boldsymbol{\mathcal{G}}')\cdot\boldsymbol{r}}\, \boldsymbol{\mathcal{A}}(\boldsymbol{r})\, e^{i(\boldsymbol{k}-\boldsymbol{\mathcal{G}})\cdot\boldsymbol{r}} = \delta_{\boldsymbol{k}\boldsymbol{k}'}\boldsymbol{\mathcal{A}}_{\boldsymbol{\mathcal{G}}-\boldsymbol{\mathcal{G}}'}, \tag{134}$$

$$\frac{1}{V}\int d^2\boldsymbol{r}\, e^{-i(\boldsymbol{k}'-\boldsymbol{\mathcal{G}}')\cdot\boldsymbol{r}}\, \mathcal{V}(\boldsymbol{r})\, e^{i(\boldsymbol{k}-\boldsymbol{\mathcal{G}})\cdot\boldsymbol{r}} = \delta_{\boldsymbol{k}\boldsymbol{k}'}\mathcal{V}_{\boldsymbol{\mathcal{G}}-\boldsymbol{\mathcal{G}}'}. \tag{135}$$

For example, for the triangular height profile, we have

$$\boldsymbol{\mathcal{A}}_{\boldsymbol{\mathcal{G}}} = \frac{1}{2}\sum_{n=1}^{3}\boldsymbol{\mathcal{A}}_n\left(ie^{-2i\phi}\delta_{\boldsymbol{\mathcal{G}},\boldsymbol{\mathcal{G}}_n} - ie^{2i\phi}\delta_{\boldsymbol{\mathcal{G}},-\boldsymbol{\mathcal{G}}_n}\right) + \overline{\boldsymbol{\mathcal{A}}}_{\boldsymbol{\mathcal{G}}}, \tag{136}$$

$$\mathcal{V}_{\boldsymbol{\mathcal{G}}} = \frac{\mathcal{V}_0}{2}\sum_{n=1}^{3}\left(e^{i(\phi+\pi/4)}\delta_{\boldsymbol{\mathcal{G}},\boldsymbol{\mathcal{G}}_n} + e^{-i(\phi+\pi/4)}\delta_{\boldsymbol{\mathcal{G}},-\boldsymbol{\mathcal{G}}_n}\right), \tag{137}$$

where $\overline{\boldsymbol{\mathcal{A}}}_{\boldsymbol{\mathcal{G}}}$ corresponds to higher harmonics that can be gauged away (i.e., they do not contribute to the curl of the pseudo vector potential) and

$$\boldsymbol{\mathcal{A}}_1 = \frac{\mathcal{B}_0}{\mathcal{G}}\begin{pmatrix}1\\0\end{pmatrix}, \qquad \boldsymbol{\mathcal{A}}_{2/3} = \frac{\mathcal{B}_0}{\mathcal{G}}\begin{pmatrix}-1/2\\ \pm\sqrt{3}/2\end{pmatrix}, \qquad \mathcal{V}_0 = -eE_z h_0, \tag{138}$$

with $\mathcal{G} = 4\pi/\sqrt{3}L$ and E_z the electric field perpendicular to the nominal graphene plane. For computational convenience, it can be preferable to use the gauge

$$\boldsymbol{\mathcal{A}}(\boldsymbol{r}) = -\hat{x}\mathcal{B}_0\sum_{n=1}^{3}\frac{\sin\left(\boldsymbol{\mathcal{G}}_n - 2\phi\right)}{\mathcal{G}_{ny}}, \tag{139}$$

which preserves the symmetries of the system up to a gradient term. The Hamiltonian becomes

$$\hat{H}_\nu = \sum_{\boldsymbol{k}}\sum_{\boldsymbol{\mathcal{G}},\boldsymbol{\mathcal{G}}'}\hat{c}^\dagger_{\nu,\boldsymbol{k}-\boldsymbol{\mathcal{G}}'}\left\{\hbar v\left[\left(\boldsymbol{k}-\boldsymbol{\mathcal{G}}\right)\delta_{\boldsymbol{\mathcal{G}}\boldsymbol{\mathcal{G}}'} + \frac{\nu e}{\hbar}\,\boldsymbol{\mathcal{A}}_{\boldsymbol{\mathcal{G}}-\boldsymbol{\mathcal{G}}'}\right]\cdot(\nu\sigma_x,\sigma_y) + \mathcal{V}_{\boldsymbol{\mathcal{G}}-\boldsymbol{\mathcal{G}}'}\right\}\hat{c}_{\nu,\boldsymbol{k}-\boldsymbol{\mathcal{G}}}, \tag{140}$$

which can be diagonalized numerically by taking a finite number of $\boldsymbol{\mathcal{G}}$ vectors. The number of reciprocal lattice vectors is then increased until the results are converged. The output of this calculation yields the energy bands $\varepsilon^\nu_{n\boldsymbol{k}}$ with eigenvectors $C^\nu_{n,\boldsymbol{k}-\boldsymbol{\mathcal{G}}}$ where n is the band index. Leaving out the valley index, the Bloch wave function becomes

$$\Psi_{n\boldsymbol{k}}(\boldsymbol{r}) = e^{i\boldsymbol{k}\cdot\boldsymbol{r}}u_{n\boldsymbol{k}}(\boldsymbol{r}), \qquad u_{n\boldsymbol{k}}(\boldsymbol{r}) = \frac{1}{\sqrt{V_c}}\sum_{\boldsymbol{\mathcal{G}}}C_{n,\boldsymbol{k}-\boldsymbol{\mathcal{G}}}\,e^{-i\boldsymbol{\mathcal{G}}\cdot\boldsymbol{r}}, \tag{141}$$

where $u_{n\boldsymbol{k}}$ are the cell-periodic functions, obeying the periodic gauge condition: $u_{n,\boldsymbol{k}+\boldsymbol{\mathcal{G}}}(\boldsymbol{r}) = e^{-i\boldsymbol{\mathcal{G}}\cdot\boldsymbol{r}}u_{n\boldsymbol{k}}(\boldsymbol{r})$ and normalization $\langle u_{n\boldsymbol{k}}|u_{m\boldsymbol{k}}\rangle_{\text{cell}} = \delta_{nm}$. For the calculation of the Berry curvature, we need to evaluate overlaps between the cell-periodic functions at neighboring $\boldsymbol{k}$ points,

$$\langle u_{n\boldsymbol{k}}|u_{n\boldsymbol{k}'}\rangle_{\text{cell}} = \frac{1}{V_c}\sum_{\boldsymbol{\mathcal{G}},\boldsymbol{\mathcal{G}}'}\left(C_{n,\boldsymbol{k}-\boldsymbol{\mathcal{G}}}\right)^* C_{n',\boldsymbol{k}'-\boldsymbol{\mathcal{G}}'}\int_{\text{cell}}d^2\boldsymbol{r}\, e^{i(\boldsymbol{\mathcal{G}}-\boldsymbol{\mathcal{G}}')\cdot\boldsymbol{r}} \tag{142}$$

$$= \sum_{\boldsymbol{\mathcal{G}}}\left(C_{n,\boldsymbol{k}-\boldsymbol{\mathcal{G}}}\right)^* C_{n',\boldsymbol{k}'-\boldsymbol{\mathcal{G}}}. \tag{143}$$

If we measure momentum and energy in units of $k_0 = 4\pi/3L$ and $\hbar v k_0$, respectively, the continuum model can be written in terms of two dimensionless parameters,

$$\frac{L}{l_0}, \qquad \frac{\mathcal{V}_0}{\hbar v k_0}, \tag{144}$$

where $l_0 = \sqrt{\hbar/e\mathcal{B}_0} \propto h_0$ is an effective magnetic length. In the following, we take the experimental values of Ref. [15] ($L = 14$ nm and $\mathcal{B}_0 = 120$ T) which gives $L/l_0 \approx 6$ and $\hbar v k_0 \approx 172$ meV, and regard $\mathcal{V}_0$ and ϕ as tunable parameters. Because this model has a chiral symmetry under simultaneous reversal of the scalar potential, $\sigma_z\mathcal{H}_\nu[\mathcal{V}]\sigma_z = -\mathcal{H}_\nu[-\mathcal{V}]$, we only need to consider the valence bands. This model symmetry implies

$$\varepsilon^\nu_{n\boldsymbol{k}}[-\mathcal{V}] = -\varepsilon^\nu_{-n,\boldsymbol{k}}[\mathcal{V}], \qquad \Omega^\nu_{n\boldsymbol{k}}[-\mathcal{V}] = \Omega^\nu_{-n,\boldsymbol{k}}[\mathcal{V}], \tag{145}$$

with n a nonzero integer such that $n > 0$ ($n < 0$) corresponds to conduction (valence) bands.

C. Berry curvature and valley Chern number

We numerically calculate the Berry curvature and valley Chern numbers. To this end, we first consider a square plaquette of area δ^2 centered at $\boldsymbol{k}$ with corners: $\boldsymbol{k}_1 = \boldsymbol{k} + \frac{\delta}{2}(-1,-1)$, $\boldsymbol{k}_2 = \boldsymbol{k} + \frac{\delta}{2}(-1,1)$, $\boldsymbol{k}_3 = \boldsymbol{k} + \frac{\delta}{2}(1,1)$, and $\boldsymbol{k}_4 = \boldsymbol{k} + \frac{\delta}{2}(1,-1)$. For a given band, we then consider the gauge-invariant product

$$\langle u_{\boldsymbol{k}_1}|u_{\boldsymbol{k}_2}\rangle\langle u_{\boldsymbol{k}_2}|u_{\boldsymbol{k}_3}\rangle\langle u_{\boldsymbol{k}_3}|u_{\boldsymbol{k}_4}\rangle\langle u_{\boldsymbol{k}_4}|u_{\boldsymbol{k}_1}\rangle = \prod_{m=1}^{4}\langle u_{\boldsymbol{k}_m}|u_{\boldsymbol{k}_{m+1}}\rangle, \tag{146}$$

where $\boldsymbol{k}_5 = \boldsymbol{k}_1$. One can show that

$$\Omega_{\boldsymbol{k}} = \lim_{\delta\to 0}\delta^{-2}\arg\prod_{m=1}^{4}\langle u_{\boldsymbol{k}_m}|u_{\boldsymbol{k}_{m+1}}\rangle, \qquad \mathrm{Tr}\, g_{\boldsymbol{k}} = -\lim_{\delta\to 0}\delta^{-2}\ln\left|\prod_{m=1}^{4}\langle u_{\boldsymbol{k}_m}|u_{\boldsymbol{k}_{m+1}}\rangle\right|, \tag{147}$$

where

$$g^{ij}_{\boldsymbol{k}} = \mathrm{Re}\left(\langle\partial_i u_{\boldsymbol{k}}|\partial_j u_{\boldsymbol{k}}\rangle\right) + \langle u_{\boldsymbol{k}}|\partial_i u_{\boldsymbol{k}}\rangle\langle u_{\boldsymbol{k}}|\partial_j u_{\boldsymbol{k}}\rangle, \tag{148}$$

is the Fubiny-Study quantum metric. For convenience, we use a Bravais grid (k_1, k_2) with $\boldsymbol{k} = k_1\boldsymbol{\mathcal{G}}_1 + k_2\boldsymbol{\mathcal{G}}_2$ where

$$\Omega_{\boldsymbol{k}} = \frac{V_c}{(2\pi)^2}F_{12}, \qquad F_{12} = i\left(\langle\partial_1 u_{\boldsymbol{k}}|\partial_2 u_{\boldsymbol{k}}\rangle - \langle\partial_2 u_{\boldsymbol{k}}|\partial_1 u_{\boldsymbol{k}}\rangle\right), \qquad \mathcal{C} = \frac{1}{2\pi}\sum_{k_1,k_2}F_{12}. \tag{149}$$

D. Phase diagrams

We focus on the highest valence band, taking into account both valleys. We numerically calculated the phase diagram in the $(\mathcal{V}_0, \phi)$ plane for the smallest energy gap to the two neighboring bands $\varepsilon_{\mathrm{gap}}$. We also calculated the bandwidth $\varepsilon_{\mathrm{width}}$, as well as the ratios $\varepsilon_{\mathrm{gap}}/\varepsilon_{\mathrm{width}}$ and $\varepsilon^2_{\mathrm{gap}}/\varepsilon_{\mathrm{width}}$. These diagrams are shown in Fig. S6. Notice that these diagrams are invariant under $(\mathcal{V}_0, \phi) \mapsto (-\mathcal{V}_0, \phi + \pi/3)$. On the phase diagram showing the energy gap, we have indicated the valley Chern numbers of the highest valence band and the lowest conduction band. The energy bands along high-symmetry lines of the SBZ for the parameters corresponding to the circle, disk, and cross in the phase diagrams, are shown in Fig. S7. In the main text, we were mainly interested in showing that the ratio $\varepsilon^2_{\mathrm{gap}}/\varepsilon_{\mathrm{width}}$ can be made large enough such that electric breakdown is absent even in the strong-field limit, i.e., the regime

$$\frac{0.66\,\mathrm{ps}}{\tau}\frac{10\,\mathrm{nm}}{L} \ll \frac{E}{\mathrm{kV/cm}} \ll \frac{\varepsilon^2_{\mathrm{gap}}}{\varepsilon_{\mathrm{width}}\mathrm{meV}}\frac{10\,\mathrm{nm}}{L}. \tag{150}$$

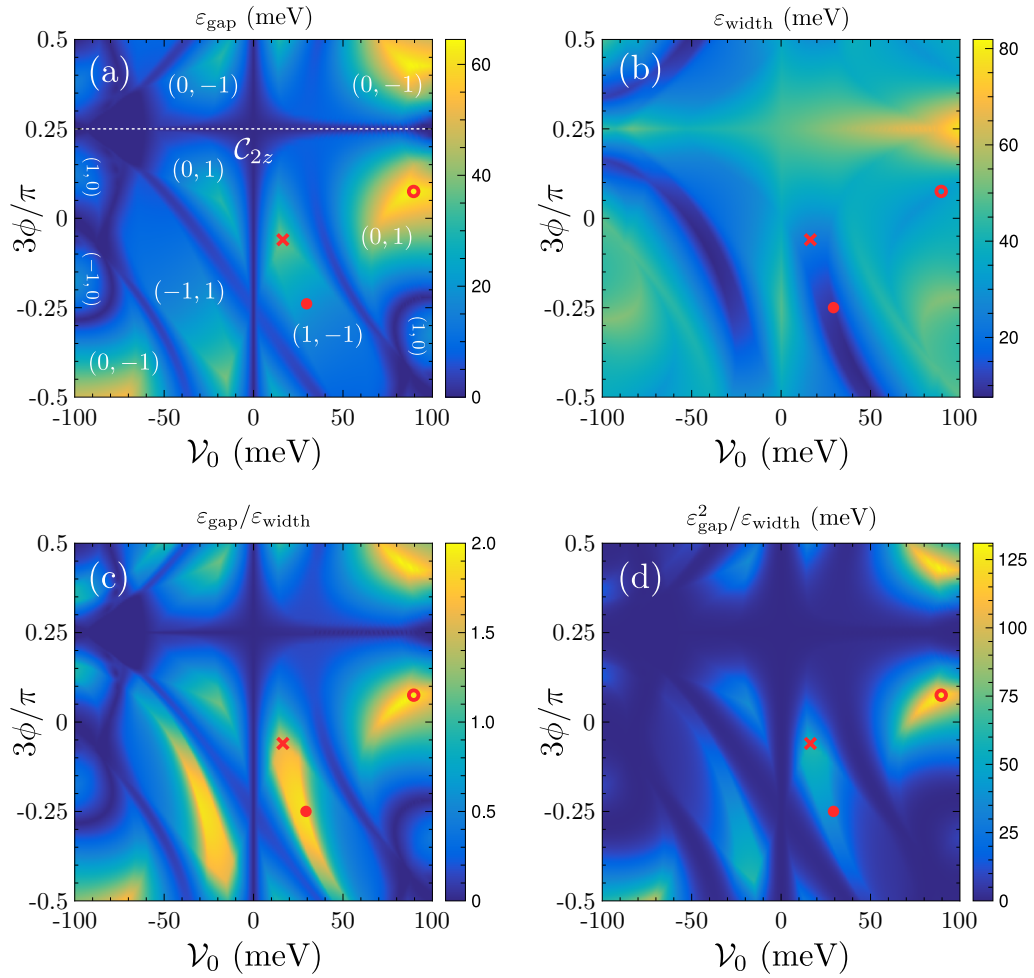

FIG. S6. (a) Phase diagram of PBG in the $(\mathcal{V}_0, \phi)$ plane. The density plot gives the smallest energy gap $\varepsilon_{\rm gap}$ of the highest valence band to other bands and the valley Chern numbers of the highest valence and lowest conduction band for valley K_+ is shown as $(\mathcal{C}_{n=-1}, \mathcal{C}_{n=+1})$. (b) Bandwidth $\varepsilon_{\rm width}$ of the highest valence band. (c) Ratio $\varepsilon_{\rm gap}/\varepsilon_{\rm width}$ for the highest valence band. (d) Ratio $\varepsilon^2_{\rm gap}/\varepsilon_{\rm width}$ for the highest valence band.

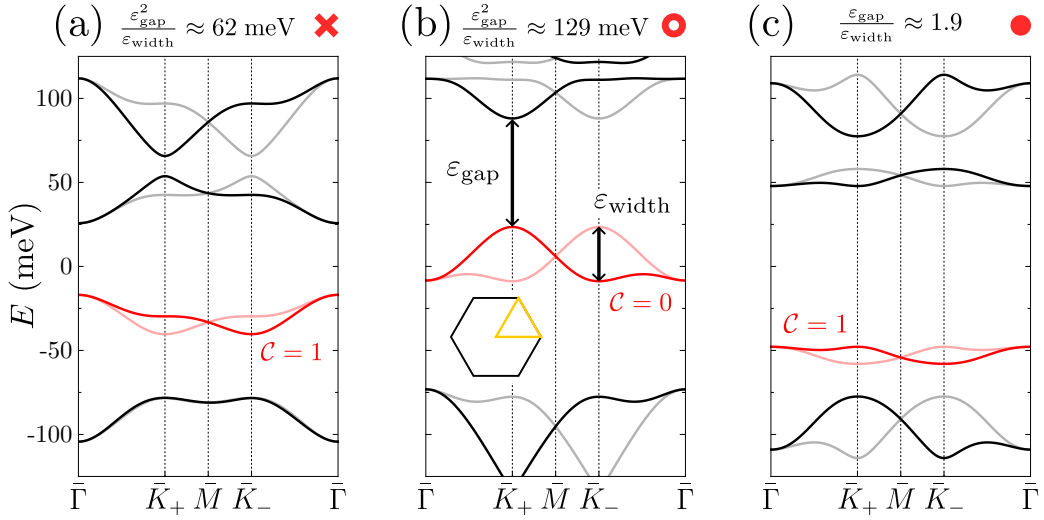

FIG. S7. Energy bands of PBG for $L/l_0 = 6$ and $\hbar v k_0 \approx 172$ meV along high-symmetry lines of the SBZ as indicated in (a). The light/dark bands correspond to valley K_+/K_- and the red band is the highest valence band. (a) $\mathcal{V}_0/\hbar v k_0 = 0.095$ and $3\phi/\pi = -0.06$. (b) $\mathcal{V}_0/\hbar v k_0 = 0.52$ and $3\phi/\pi = 0.075$. (c) $\mathcal{V}_0/\hbar v k_0 = 0.17$ and $3\phi/\pi = -0.25$.

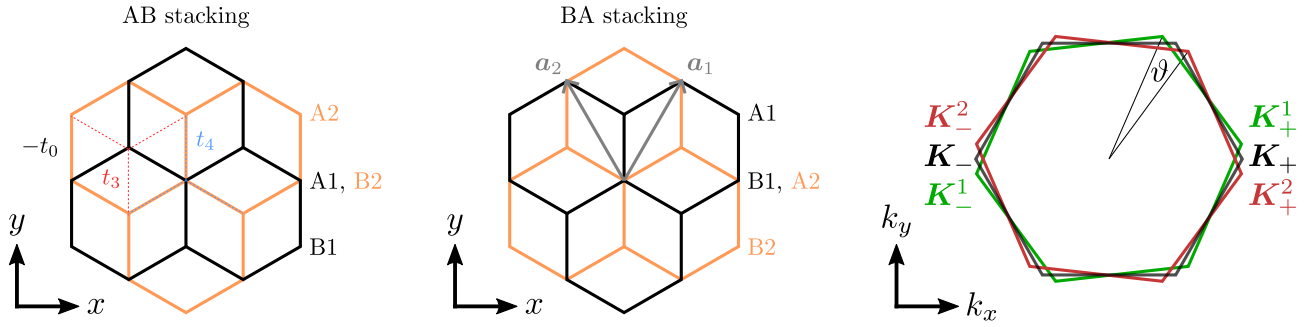

FIG. S8. Different stacking configurations of Bernal bilayer graphene and the first BZ of graphene with the two valleys $\boldsymbol{K}_\pm = (\pm 4\pi/3a, 0)$ and the rotated zone corners of the two bilayers $\boldsymbol{K}_\pm^1$ and $\boldsymbol{K}_\pm^2$. On the left, we indicate the intralayer nearest-neighbor hopping $-t_0$, and the skew interlayer hoppings t_3 (intersublattice) and t_4 (intrasublattice) with dashed lines.

IV. TWISTED DOUBLE BILAYER GRAPHENE

We give an overview of the continuum model for twisted double bilayer graphene, following Ref. [16]. Before we proceed, we give a short review of the continuum theory of Bernal bilayer graphene.

A. Bernal bilayer graphene

We consider a Bernal-stacked bilayer graphene. The sublattices on the first layer are denoted as A_1 and B_1, and those on the second layer as A_2 and B_2. We define AB-stacked (BA-stacked) bilayer graphene as the stacking configuration where the atoms of A_1 (B_1) and B_2 (A_1) eclipse one another. This is illustrated in Fig. S8.

Following [17], we use a lattice model for Bernal bilayer graphene that takes into account intralayer nearest-neighbor hopping with amplitude $-t_0$, interlayer hopping between eclipsing atoms t_1, as well as skew interlayer hopping t_3 (intersublattice) and t_4 (intrasublattice), and a sublattice staggering potential δ. The latter is due to the different environment of the eclipsing atoms. The point group of Bernal bilayer graphene is $D_{3d} = \langle \mathcal{C}_{3z}, \mathcal{C}_{2y}, \mathcal{I} \rangle$ where $\mathcal{I}$ is spatial inversion $[(\boldsymbol{r}, z) \mapsto (-\boldsymbol{r}, -z)]$. Applying an interlayer bias potential breaks inversion symmetry and reduces the point group to $D_3 = \langle \mathcal{C}_{3z}, \mathcal{C}_{2y} \rangle$.

The corresponding Bloch Hamiltonian of AB Bernal bilayer graphene is given by

$$h_{\mathrm{AB}}(\boldsymbol{k}) = \begin{pmatrix} U_1+\delta & -t_0 f(\boldsymbol{k})^* & t_4 f(\boldsymbol{k}) & t_1 \\ -t_0 f(\boldsymbol{k}) & U_1 & t_3 f(\boldsymbol{k})^* & t_4 f(\boldsymbol{k}) \\ t_4 f(\boldsymbol{k})^* & t_3 f(\boldsymbol{k}) & U_2 & -t_0 f(\boldsymbol{k})^* \\ t_1 & t_4 f(\boldsymbol{k})^* & -t_0 f(\boldsymbol{k}) & U_2+\delta \end{pmatrix} \equiv \begin{pmatrix} h_0(\boldsymbol{k})+U_1 & g^\dagger(\boldsymbol{k}) \\ g(\boldsymbol{k}) & h_0'(\boldsymbol{k})+U_2 \end{pmatrix}, \tag{151}$$

and thus

$$h_{\mathrm{BA}}(\boldsymbol{k}) = \begin{pmatrix} h_0'(\boldsymbol{k})+U_1 & g(\boldsymbol{k}) \\ g^\dagger(\boldsymbol{k}) & h_0(\boldsymbol{k})+U_2 \end{pmatrix}, \tag{152}$$

where

$$f(\boldsymbol{k}) = 1 + e^{i\boldsymbol{k}\cdot\boldsymbol{a}_1} + e^{i\boldsymbol{k}\cdot\boldsymbol{a}_2}, \tag{153}$$

and $\boldsymbol{a}_{1/2} = a(\pm 1/2, \sqrt{3}/2)$ with $a \approx 0.246$ nm, see Fig. S8. The sign difference between the intralayer and interlayer hoppings comes from the relative sign of the overlap of p_z orbitals within and between the layers. We take the following values for the hopping constants $t_0 = 2.7$ eV (below we use an effective t_0), $t_1 = 0.4$ eV, $t_3 = 0.32$ eV, $t_4 = 0.044$ eV, and $\delta = 0.05$ eV [16]. Defining the two valleys as $\boldsymbol{K}_\pm = (\pm 4\pi/3a, 0)$, we find

$$f(\boldsymbol{k} + \boldsymbol{K}_\pm) \simeq -\frac{\sqrt{3}}{2} a\,(\pm k_x + i k_y)\,, \tag{154}$$

up to first order in $|\boldsymbol{k}|$. Hence, if we place the origin of the momentum at $\boldsymbol{K}_\pm$,

$$h_{0\nu}(\boldsymbol{k}) \simeq \begin{bmatrix} \delta & \hbar v\,(\nu k_x - i k_y) \\ \hbar v\,(\nu k_x + i k_y) & 0 \end{bmatrix}, \qquad h_{0\nu}'(\boldsymbol{k}) \simeq \begin{bmatrix} 0 & \hbar v\,(\nu k_x - i k_y) \\ \hbar v\,(\nu k_x + i k_y) & \delta \end{bmatrix}, \tag{155}$$

where $\nu = \pm 1$ corresponds to valley $\boldsymbol{K}_\pm$, respectively, and $\hbar v = \sqrt{3} t_0 a/2$. In our TDBG calculations, we follow Refs. [18] and [16] and take a smaller value of $\hbar v \approx 525.308$ meV nm, corresponding to an effective t_0 of 2.1354 eV, due to longer-range intersublattice hopping within a single graphene layer in their model. We also have

$$g_\nu(\boldsymbol{k}) \simeq \begin{bmatrix} -\hbar v_4 \left(\nu k_x - i k_y\right) & -\hbar v_3 \left(\nu k_x + i k_y\right) \\ t_1 & -\hbar v_4 \left(\nu k_x - i k_y\right) \end{bmatrix}, \tag{156}$$

with $\hbar v_3 = \sqrt{3} t_3 a/2$ and $\hbar v_4 = \sqrt{3} t_4 a/2$.

B. Twisted double bilayer graphene

We now consider twisted double bilayer graphene (TDBG). Notice that in the absence (presence) of an interlayer bias, the point group of Bernal TDBG is given by D_3 (C_3) [16]. Rotating the Bernal bilayer graphene by an angle ϑ is equivalent to sending

$$f(\boldsymbol{k}) \mapsto 1 + e^{i \boldsymbol{k} \cdot R(\vartheta) \boldsymbol{a}_1} + e^{i \boldsymbol{k} \cdot R(\vartheta) \boldsymbol{a}_2} = f(R(-\vartheta)\boldsymbol{k}), \tag{157}$$

in the lattice model, with $R(\vartheta)$ the 2×2 rotation matrix. Hence the rotated Dirac points are located at $R(\vartheta)\boldsymbol{K}_\pm$. We construct TDBG by first stacking two Bernal bilayers directly on top of each other, and then rotating the first bilayer by $+\vartheta/2$ and the second bilayer by $-\vartheta/2$. Only the second and third graphene layers are coupled by the interlayer moiré potential

$$T_\nu(\boldsymbol{r}) = T_{\nu 0} + T_{\nu 1} e^{i \nu \boldsymbol{\mathcal{G}}_1 \cdot \boldsymbol{r}} + T_{\nu 2} e^{i \nu \boldsymbol{\mathcal{G}}_2 \cdot \boldsymbol{r}}, \tag{158}$$

where $\boldsymbol{\mathcal{G}}_{1/2} = (4\pi/\sqrt{3}L)(\pm 1/2, \sqrt{3}/2)$ are moiré reciprocal lattice vectors, and

$$T_{\nu n} = w_0 \sigma_0 + w_1 \left[\cos\left(\frac{2\pi n}{3}\right) \sigma_x + \nu \sin\left(\frac{2\pi n}{3}\right) \sigma_y \right], \tag{159}$$

with $w_0 = 79.7$ meV and $w_1 = 97.5$ meV the AA and AB interlayer moiré amplitudes [16, 19].

For AB–AB stacked TDBG, we have

$$\hat{H}_\nu^{\text{AB–AB}} = \int d^2 \boldsymbol{r}\, \hat{\psi}_\nu^\dagger(\boldsymbol{r})\, \mathcal{H}_\nu^{\text{AB–AB}}(-i\nabla)\, \hat{\psi}_\nu(\boldsymbol{r}), \tag{160}$$

with $\hat{\psi}_\nu = (\hat{\psi}_{\nu,A1}, \hat{\psi}_{\nu,B1}, \hat{\psi}_{\nu,A2}, \hat{\psi}_{\nu,B2}, \hat{\psi}_{\nu,A3}, \hat{\psi}_{\nu,B3}, \hat{\psi}_{\nu,A4}, \hat{\psi}_{\nu,B4})^t$ and

$$\mathcal{H}_\nu^{\text{AB–AB}}(-i\nabla) = \begin{pmatrix} h_{0\nu}(\boldsymbol{k}_1) + U_1 & g_\nu^\dagger(\boldsymbol{k}_1) & 0 & 0 \\ g_\nu(\boldsymbol{k}_1) & h'_{0\nu}(\boldsymbol{k}_1) + U_2 & T_\nu^\dagger(\boldsymbol{r}) & 0 \\ 0 & T_\nu(\boldsymbol{r}) & h_{0\nu}(\boldsymbol{k}_2) + U_3 & g_\nu^\dagger(\boldsymbol{k}_2) \\ 0 & 0 & g_\nu(\boldsymbol{k}_2) & h'_{0\nu}(\boldsymbol{k}_2) + U_4 \end{pmatrix}, \tag{161}$$

where $\boldsymbol{k}_{1/2} = R(\mp\vartheta/2)\left(-i\nabla - \nu \boldsymbol{q}_{1/2}\right)$ with $\boldsymbol{q}_{1/2} = k_\vartheta(\sqrt{3}/2, \pm 1/2)$ and $k_\vartheta = 4\pi/3L$ with $L = a/2\sin(\vartheta/2)$ the moiré lattice constant. Here we have placed the origin of momentum in the center of the moiré Brillouin zone (MBZ). We further take $U_1 = U/2$, $U_2 = U/6$, $U_3 = -U/6$, and $U_4 = -U/2$, such that U is the bias between the topmost and bottommost layer. Similarly, we have for AB–BA stacked TDBG,

$$\hat{H}_\nu^{\text{AB–BA}} = \int d^2 \boldsymbol{r}\, \hat{\psi}_\nu^\dagger(\boldsymbol{r})\, \mathcal{H}_\nu^{\text{AB–BA}}(-i\nabla)\, \hat{\psi}_\nu(\boldsymbol{r}), \tag{162}$$

with

$$\mathcal{H}_\nu^{\text{AB–BA}}(-i\nabla) = \begin{pmatrix} h_{0\nu}(\boldsymbol{k}_1) + U_1 & g_\nu^\dagger(\boldsymbol{k}_1) & 0 & 0 \\ g_\nu(\boldsymbol{k}_1) & h'_{0\nu}(\boldsymbol{k}_1) + U_2 & T_\nu^\dagger(\boldsymbol{r}) & 0 \\ 0 & T_\nu(\boldsymbol{r}) & h'_{0\nu}(\boldsymbol{k}_2) + U_3 & g_\nu(\boldsymbol{k}_2) \\ 0 & 0 & g_\nu^\dagger(\boldsymbol{k}_2) & h_{0\nu}(\boldsymbol{k}_2) + U_4 \end{pmatrix}. \tag{163}$$

The Hamiltonian is diagonalized by Fourier transform,

$$\hat{\psi}_\nu(\boldsymbol{r}) = \frac{1}{\sqrt{V}} \sum_{\boldsymbol{k}} \sum_{\boldsymbol{\mathcal{G}}} e^{i(\boldsymbol{k} - \boldsymbol{\mathcal{G}}) \cdot \boldsymbol{r}} \hat{c}_{\nu, \boldsymbol{k} - \boldsymbol{\mathcal{G}}}, \tag{164}$$

where the sum over $\boldsymbol{k}$ only runs over the MBZ and $\boldsymbol{\mathcal{G}}$ is a reciprocal lattice vector of the moiré. Note that every wave vector has a unique decomposition as $\boldsymbol{k}-\boldsymbol{\mathcal{G}}$. We have

$$\frac{1}{V}\int d^2\boldsymbol{r}\, e^{-i(\boldsymbol{k}'-\boldsymbol{\mathcal{G}}')\cdot\boldsymbol{r}}\, e^{i(\boldsymbol{k}-\boldsymbol{\mathcal{G}})\cdot\boldsymbol{r}} = \delta_{\boldsymbol{k}\boldsymbol{k}'}\delta_{\boldsymbol{\mathcal{G}}\boldsymbol{\mathcal{G}}'}, \tag{165}$$

$$\frac{1}{V}\int d^2\boldsymbol{r}\, e^{-i(\boldsymbol{k}'-\boldsymbol{\mathcal{G}}')\cdot\boldsymbol{r}}\, T_\nu(\boldsymbol{r})\, e^{i(\boldsymbol{k}-\boldsymbol{\mathcal{G}})\cdot\boldsymbol{r}} = \delta_{\boldsymbol{k}\boldsymbol{k}'}T_{\nu,\boldsymbol{\mathcal{G}}-\boldsymbol{\mathcal{G}}'}, \tag{166}$$

with

$$T_{\nu,\boldsymbol{\mathcal{G}}} = T_{\nu 0}\delta_{\boldsymbol{\mathcal{G}},\boldsymbol{0}} + T_{\nu 1}\delta_{\boldsymbol{\mathcal{G}},\nu\boldsymbol{\mathcal{G}}_1} + T_{\nu 2}\delta_{\boldsymbol{\mathcal{G}},\nu\boldsymbol{\mathcal{G}}_2}. \tag{167}$$

C. Phase diagrams

For TDBG we focus on the lowest conduction band. We find that the highest valence band lacks a global energy gap to the remote bands for most of the parameter regime that we considered. We numerically calculated the phase diagram in the (ϑ, U) plane for the smallest energy gap to the two neighboring bands ε_{gap}. We also calculated the bandwidth $\varepsilon_{\text{width}}$, as well as the ratios $\varepsilon_{\text{gap}}/\varepsilon_{\text{width}}$ and $\varepsilon_{\text{gap}}^2/\varepsilon_{\text{width}}$. These diagrams are shown in Fig. S9 for AB–AB TDBG and in Fig. S11 for AB–BA TDBG, for the lowest conduction band. On the phase diagram showing the energy gap, we have indicated the valley Chern number of the lowest conduction band. The energy bands along high-symmetry lines of the SBZ for the parameters corresponding to the cross in the phase diagrams are shown in Fig. S10 for AB–AB TDBG and in Fig. S12 for AB–BA TDBG.

[1] M.-C. Chang and Q. Niu, Berry Phase, Hyperorbits, and the Hofstadter Spectrum, Phys. Rev. Lett. **75**, 1348 (1995).
[2] G. Sundaram and Q. Niu, Wave-packet dynamics in slowly perturbed crystals: Gradient corrections and Berry-phase effects, Phys. Rev. B **59**, 14915 (1999).
[3] Y. Gao, S. A. Yang, and Q. Niu, Field induced positional shift of bloch electrons and its dynamical implications, Phys. Rev. Lett. **112**, 166601 (2014).
[4] V. o. T. Phong and E. J. Mele, Quantum geometric oscillations in two-dimensional flat-band solids, Phys. Rev. Lett. **130**, 266601 (2023).
[5] L. D. Landau and E. M. Lifshitz, *Theory of Elasticity* (Pergamon Press, 1970).
[6] F. Guinea, B. Horovitz, and P. Le Doussal, Gauge field induced by ripples in graphene, Phys. Rev. B **77**, 205421 (2008).
[7] V. T. Phong and E. J. Mele, Boundary Modes from Periodic Magnetic and Pseudomagnetic Fields in Graphene, Phys. Rev. Lett. **128**, 176406 (2022).
[8] H. Suzuura and T. Ando, Phonons and electron-phonon scattering in carbon nanotubes, Phys. Rev. B **65**, 235412 (2002).
[9] J. L. Mañes, Symmetry-based approach to electron-phonon interactions in graphene, Phys. Rev. B **76**, 045430 (2007).
[10] F. Guinea, A. K. Geim, M. I. Katsnelson, and K. S. Novoselov, Generating quantizing pseudomagnetic fields by bending graphene ribbons, Phys. Rev. B **81**, 035408 (2010).
[11] M. Vozmediano, M. Katsnelson, and F. Guinea, Gauge fields in graphene, Phys. Rep. **496**, 109 (2010).
[12] F. de Juan, J. L. Mañes, and M. A. H. Vozmediano, Gauge fields from strain in graphene, Phys. Rev. B **87**, 165131 (2013).
[13] C. De Beule, V. T. Phong, and E. J. Mele, Network model for periodically strained graphene, Phys. Rev. B **107**, 045405 (2023).
[14] A. H. Castro Neto, F. Guinea, N. M. R. Peres, K. S. Novoselov, and A. K. Geim, The electronic properties of graphene, Rev. Mod. Phys. **81**, 109 (2009).
[15] J. Mao, S. P. Milovanović, M. Anđelković, X. Lai, Y. Cao, K. Watanabe, T. Taniguchi, L. Covaci, F. M. Peeters, A. K. Geim, Y. Jiang, and E. Y. Andrei, Evidence of flat bands and correlated states in buckled graphene superlattices, Nature **584**, 215 (2020).
[16] M. Koshino, Band structure and topological properties of twisted double bilayer graphene, Phys. Rev. B **99**, 235406 (2019).
[17] E. McCann and M. Koshino, The electronic properties of bilayer graphene, Reports on Progress in Physics **76**, 056503 (2013).
[18] P. Moon and M. Koshino, Optical absorption in twisted bilayer graphene, Phys. Rev. B **87**, 205404 (2013).
[19] M. Koshino, N. F. Q. Yuan, T. Koretsune, M. Ochi, K. Kuroki, and L. Fu, Maximally Localized Wannier Orbitals and the Extended Hubbard Model for Twisted Bilayer Graphene, Phys. Rev. X **8**, 031087 (2018).

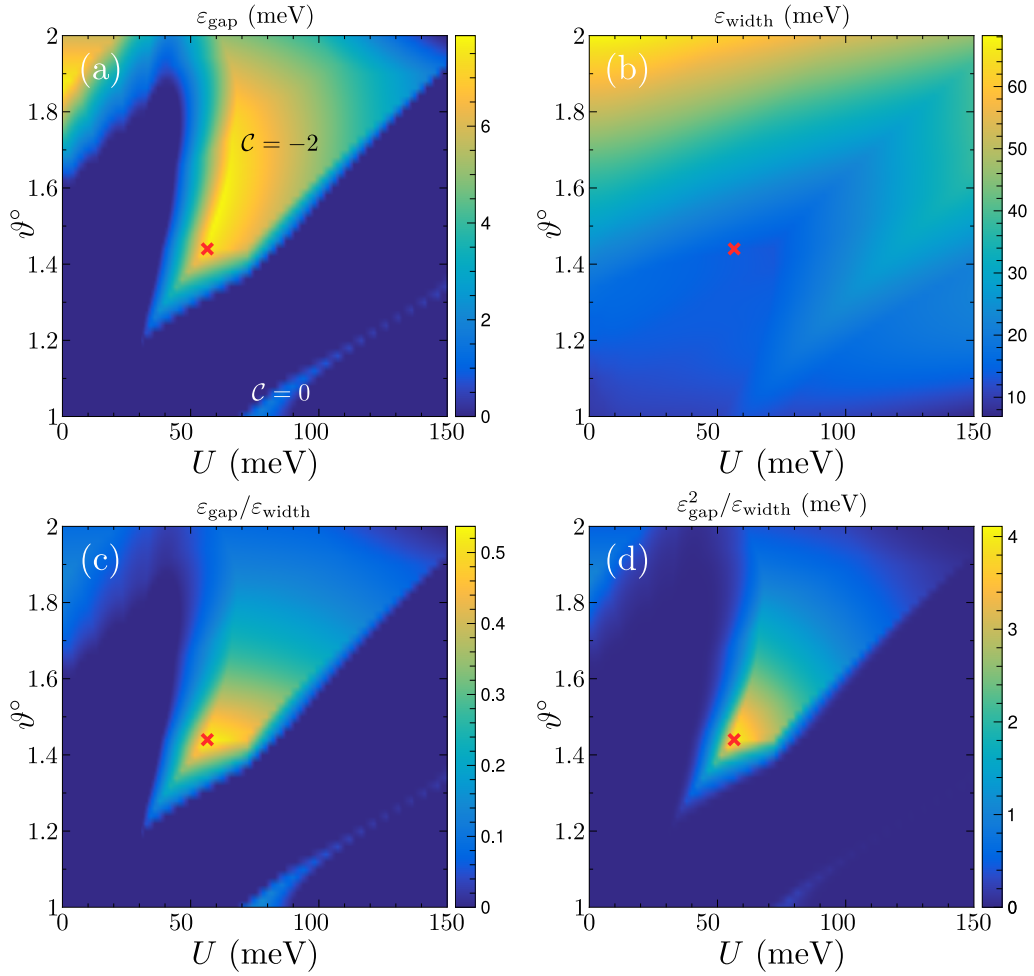

FIG. S9. (a) Phase diagram of AB–AB TDBG in the (U, ϑ) plane. The density plot gives the smallest energy gap $\varepsilon_{\rm gap}$ of the lowest conduction band to other bands and the valley Chern number for valley K_+. (b) Bandwidth $\varepsilon_{\rm width}$ of the lowest conduction band. (c) Ratio $\varepsilon_{\rm gap}/\varepsilon_{\rm width}$ for the lowest conduction band. (d) Ratio $\varepsilon^2_{\rm gap}/\varepsilon_{\rm width}$ for the lowest conduction band.

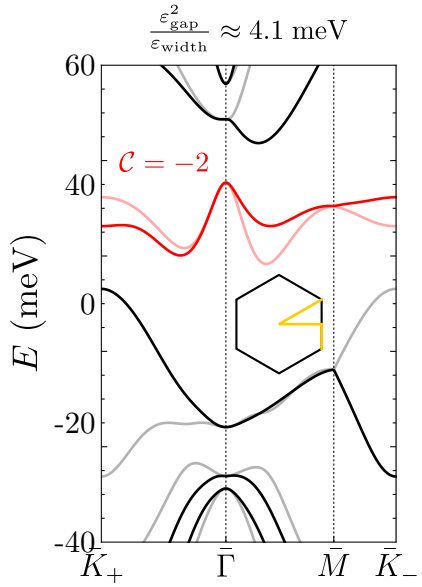

FIG. S10. Energy bands of AB–AB TDBG for $\vartheta = 1.44^\circ$ and $U = 56.5$ meV, i.e., the cross in Fig. S9 along high-symmetry lines of the SBZ as indicated. Light/dark bands correspond to valley K_+/K_- and the red band is the lowest conduction band.

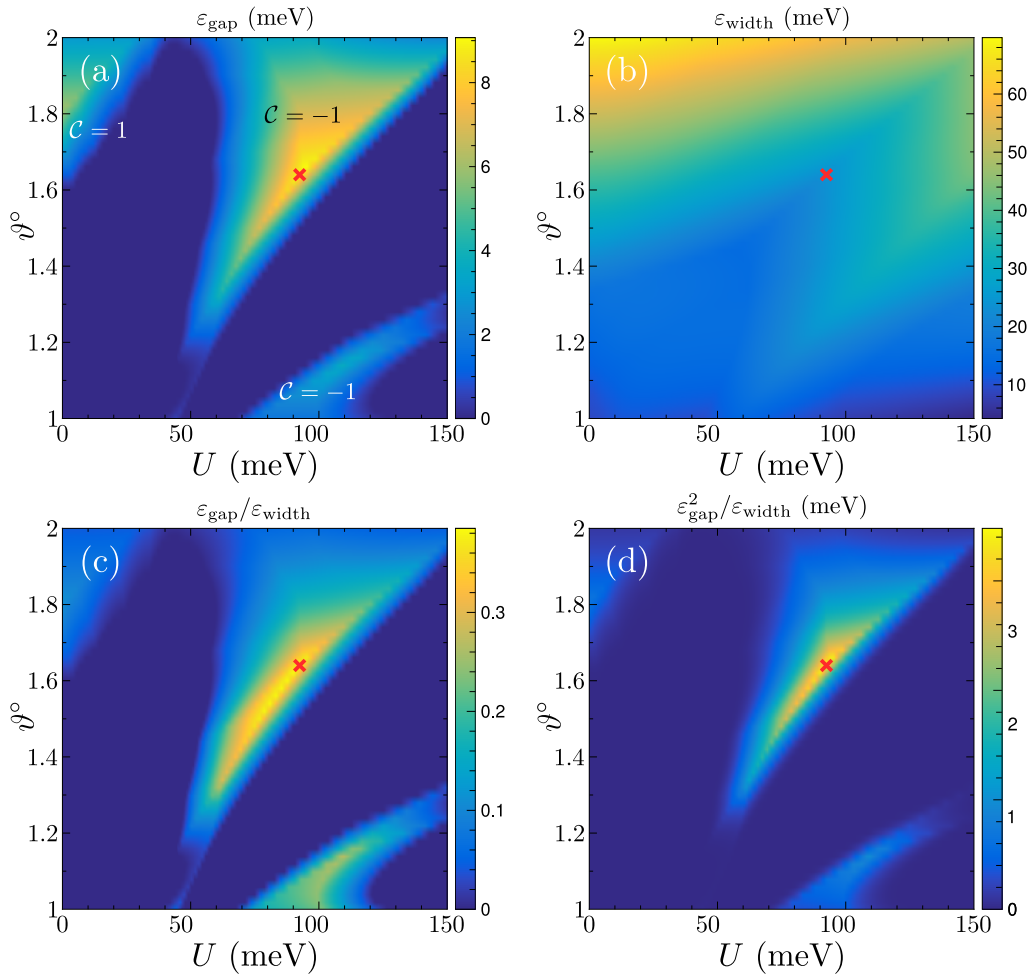

FIG. S11. (a) Phase diagram of AB–BA TDBG in the (U, ϑ) plane. The density plot gives the smallest energy gap $\varepsilon_{\rm gap}$ of the lowest conduction band to other bands and the valley Chern number for valley K_+. (b) Bandwidth $\varepsilon_{\rm width}$ of the lowest conduction band. (c) Ratio $\varepsilon_{\rm gap}/\varepsilon_{\rm width}$ for the lowest conduction band. (d) Ratio $\varepsilon^2_{\rm gap}/\varepsilon_{\rm width}$ for the lowest conduction band.

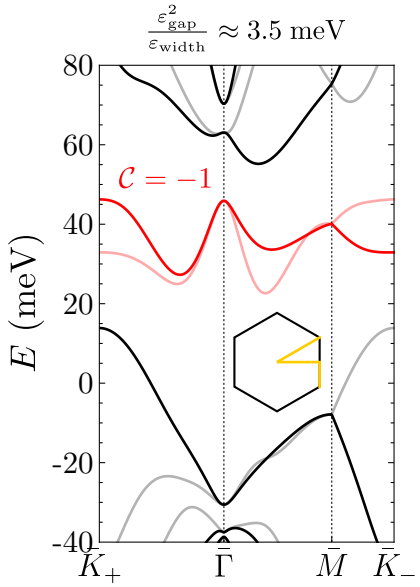

FIG. S12. Energy bands of AB–BA TDBG for $\vartheta = 1.64^\circ$ and $U = 92.5$ meV, i.e., the cross in Fig. S11, along high-symmetry lines of the SBZ as indicated. Light/dark bands correspond to valley K_+/K_- and the red band is the lowest conduction band.